



UNIVERSIDADE D  
COIMBRA

André Valentim Costa Fontes

**PRODUCTION AND CHARACTERIZATION OF  
SHAPE MEMORY FILMS FOR  
MICROELECTROMECHANICAL SYSTEMS**

**Dissertation in the context of the Master Degree in Mechanical Engineering,  
specialization in Production and Design, advised by Doctors Ana Sofia Figueira  
Ramos and Patrícia Freitas Rodrigues, and presented to the Department of  
Mechanical Engineering of the Faculty of Science and Technology of the  
University of Coimbra.**

September of 2023



1 2



9 0

FACULDADE DE  
CIÊNCIAS E TECNOLOGIA  
UNIVERSIDADE DE  
COIMBRA

# **Production and characterization of shape memory films for microelectromechanical systems**

A dissertation submitted in partial fulfillment of the requirements for the degree of Master in Mechanical Engineering in the specialty of Production and Design.

## **Produção e caracterização de filmes com memória de forma para sistemas microeletromecânicos**

Author

**André Valentim Costa Fontes**

Advisors

**Professora Ana Sofia Ramos**

**Investigadora Patrícia Freitas Rodrigues**

Committee

Chair                    **Doutor Ricardo Gil Henriques Serra**  
Researcher at the University of Coimbra

Member                **Doutor Diogo Albano Cavaleiro Ventura de Carvalho**  
Researcher at the University of Coimbra

Advisor                 **Doutora Patrícia Freitas Rodrigues**  
Researcher at the University of Coimbra

**Coimbra, September, 2023**



I have no special talent, I am only passionately curious.

Albert Einstein



## ACKNOWLEDGEMENTS

The current dissertation wouldn't be possible without the support of those who directly or indirectly contributed to its conclusion. So, I'm left to thank each and every one who was part of it:

To the teachers **Ana Sofia Ramos** and **Patrícia Freitas Rodrigues** who guided and encouraged me; for their orientation, opinions, criticism, as well as for their availability and collaboration on the solutioning of questions that unfolded along the development of this work.

To Doctor **Rui Martins** for his assistance, time and expertise.

To the Doctors **Francisco Braz Fernandes** and **Daniel Gatões**, and to the Masters **Luiz Cacho** and **Bernardo Alves** for their kindness and accessibility on enabling better characterization techniques enriching this dissertation.

Last but not least, to my **family**, **girlfriend** and **friends** for the continuous support on this phase, as well as their patience, appreciation, companionship and words of support.





## Abstract

Shape memory alloys, namely NiTi, are unique materials with exceptional functional properties that have been rising interest and increased popularity over the last decades. They have the potential to unlock groundbreaking solutions in several development areas, such as microelectromechanical systems (MEMS), where these distinct alloys can solve complex challenges with simple applications.

The main objective of this dissertation is to produce NiTi shape memory alloys in the form of films via two sputtering deposition strategies (NiTi target and pure Ti and Ni targets), while varying deposition parameters such as, pressure, power, time, and substrates' rotation speed. The influence of these deposition parameters on the properties of monolithic and multilayer films was studied. For this purpose, several characterization techniques were used: Profilometry, Energy Dispersive X-ray Spectroscopy, Scanning Electron Microscopy, X-Ray Diffraction, Differential Scanning Calorimetry, and Nanoindentation. As the primary goal is the application of these films in MEMS, the desired functional property is superelasticity, and thus nickel-rich films are required.

Upon completion of this thesis, several austenite crystalline superelastic films were produced with rather low heat treatment temperatures, in which the quantity of precipitates present was associated with the nickel content. Furthermore, among the films produced, some are superelastic with exceptionally high nickel content. In addition, it was possible to correlate the varied deposition parameters with the films' chemical composition, specific morphological features, structure, and thermophysical and mechanical properties, providing advances in material science and microelectromechanical systems.

**Keywords:** Shape Memory Alloys (SMAs), NiTi, Microelectromechanical systems (MEMS), Superelasticity, Austenite, Nickel content.



## Resumo

Ligas com memória de forma, nomeadamente NiTi, são materiais únicos com propriedades funcionais excepcionais que têm despertado interesse e popularidade acrescida ao longo das últimas décadas. Estas têm o potencial de apresentar soluções inovadoras em várias áreas de desenvolvimento, sendo que estes materiais se distinguem quando aplicados em sistemas microeletromecânicos, onde podem resolver desafios complexos com aplicações simples.

O objetivo desta dissertação é a produção de ligas de memória de forma de NiTi na forma de filmes a partir da técnica de pulverização catódica a partir de duas estratégias de deposição distintas (alvo NiTi ou alvos Ti e Ni independentes), variando parâmetros de deposição tais como a pressão, potência, tempo e velocidade de rotação. Foi estudado o impacto de várias combinações dos parâmetros de deposição. Com este intuito, várias técnicas de caracterização foram usadas: Perfilometria, Microscopia Eletrónica de Varrimento, Difração de Raios X, Espectroscopia de Raios X por Energia Dispersiva e Nanoindentação. Dada a meta principal ser a aplicação dos filmes em sistemas microeletromecânicos, a propriedade funcional desejada é a superelasticidade, sendo assim necessários filmes ricos em níquel.

Após conclusão do trabalho, vários filmes austeníticos superelásticos foram produzidos com temperaturas de tratamento térmico relativamente baixas, sendo que a quantidade de precipitados presentes foi correlacionada com o teor de níquel. De entre os filmes produzidos, alguns têm teores de níquel excepcionalmente elevados. Além disso, foi possível correlacionar os parâmetros de deposição com a composição química, morfologia específica, estrutura, propriedades termofísicas e propriedades mecânicas dos filmes, permitindo avanços no estudo da ciência de materiais e de sistemas microeletromecânicos.

**Palavras-chave:** Ligas com memória de forma, NiTi, Sistemas microeletromecânicos, Superelasticidade, Austenite, Teor de níquel.



---

## Contents

LIST OF FIGURES .....	ix
LIST OF TABLES.....	xi
LIST OF SIMBOLS .....	xiii
List of Symbols.....	xiii
Acronyms/Abbreviations.....	xiv
1. INTRODUCTION .....	1
2. STATE OF ART.....	3
2.1. Shape Memory Alloys .....	3
2.2. NiTi Shape Memory Alloys.....	3
2.2.1. NiTi Film Composition .....	3
2.2.2. Shape Memory Effect.....	5
2.2.3. Superelasticity Effect.....	7
2.2.4. Ni-Rich NiTi Alloys .....	7
2.3. NiTi Thin Films .....	8
2.4. Applications .....	13
3. MATERIALS AND METHODS .....	19
3.1. Materials .....	19
3.1.1. Substrates.....	19
3.1.2. Substrate Holders.....	19
3.1.3. Targets .....	19
3.2. Methods.....	20
3.2.1. Deposition Technique.....	20
3.2.2. Deposition Equipment .....	20
3.2.3. Deposition Conditions .....	21
3.2.4. Post Deposition Treatments.....	22
3.2.5. Characterization Techniques .....	23
4. RESULTS AND DISCUSSION.....	29
4.1. Chemical, morphological, structural and thermophysical characterization of the as-deposited films .....	29
4.1.1. Energy Dispersive X-Ray Spectroscopy .....	29
4.1.2. Scanning Electron Microscopy.....	30
4.1.3. X-ray diffraction.....	33
4.1.4. Differential Scanning Calorimetry .....	34
4.2. Morphological, structural and thermophysical characterization of heat treated films .....	36
4.2.1. Scanning Electron Microscopy after heat treatment.....	36
4.2.2. X-Ray Diffraction.....	37
4.2.3. Differential Scanning Calorimetry after heat treatment .....	39
4.3. Mechanical Properties.....	41
5. CONCLUSIONS .....	47

Future Work ..... 49  
REFERENCES..... 51

---

## LIST OF FIGURES

Figure 1- Ni-Ti phase diagram with emphasis on Ni-rich lower temperature section [5].....	4
Figure 2- Representation for the appearance of superelasticity and shape memory effect [1]. .....	4
Figure 3- Influence of the nominal Ni concentration on the measured $M_s$ temperature and calculated $T_0$ temperature (calculated according to Tong and Wayman for a given film [6].....	5
Figure 4- Crystal transformations in Superelasticity Effect (left) and Memory Shape Effect (right) [7]. .....	6
Figure 5- Paper Clip made of a SMA showing the Shape Memory Effect [8].....	6
Figure 6- Glasses made of a SMA showing the superelasticity effect. ....	7
Figure 7- Microstructure zone diagram for metal films deposited by magnetron sputtering where $T_m$ is the coating material melting point and $T$ is the substrate temperature [16]. .....	11
Figure 8- XRD diffractograms for Ni/Ti multilayer thin films with different periods at a) 300, b) 375, c) 400 and d) 450 °C. Substrate diffraction peaks are labelled with “S” [4].....	12
Figure 9- Hardness of Ag/Co multilayer films as a function of the period [33]. ....	13
Figure 10- Rotary endodontic instruments [34]. ....	13
Figure 11- NiTi arch wires. ....	14
Figure 12- (a) Cervical spine implantation; (b) lumbar spine implantation; (c) intervertebral fusion device and (d) acetabular cup (hip implant) [36]. ....	14
Figure 13- Model of an earthquake proof bridge that uses NiTi alloy materials [38].....	15
Figure 14- Displacement measurement testing on a NiTi wire [40] .....	15
Figure 15- Schematic of a micropump and the corresponding NiTi/silicon driving diaphragm [42]. .....	16
Figure 16- (a-d) Photographs of the different stages of activation of the microgripper (upper images) and wire’s shape set configuration (lower image) [43].....	16
Figure 17- RoBeetle and corresponding schematics and detailed views [45].....	17
Figure 18- Deposition equipment Hartec of DEM. ....	21
Figure 19- IPN SEM equipment. ....	24
Figure 20- DESY PETRAIII: High Energy X-Ray Diffraction [47].....	25
Figure 21- DEM Nanoindentation equipment. ....	27
Figure 22- SEM surface images of as-deposited films: a) M0.3_1000, b) M0.3_1700, c) M0.5_1000, d) M0.3_1000t, e) ML_4, f) ML_60.....	30

Figure 23- SEM cross-section images of as-deposited films: a) M0.3\_1000, b) M0.3\_1700, c) M0.5\_1000, d) M0.3\_1000t, e) ML\_4, f) ML\_60. .... 32

Figure 24- SEM cross-section image (higher magnification) of as-deposited films: a) M0.3\_1000 and ..... 33

Figure 25- XRD diffractograms of as-deposited monolithic films: a) M0.3\_1000 (conventional XRD) and b) M0.3\_1700 (synchrotron energy XRD). .... 34

Figure 26- XRD diffractograms of as-deposited multilayer ML\_60 film: a) conventional XRD and b) synchrotron energy XRD. .... 34

Figure 27- DSC ramp of film M0.3\_1700 during heat treatment. .... 35

Figure 28- SEM surface images of heat treated films: a) M0.3\_1000 and b) ML\_60. .... 36

Figure 29- SEM cross-section image of heat treated films: a) M0.3\_1700 and b) ML\_60. 37

Figure 30- Synchrotron XRD diffractograms of heat treated monolithic films: a) M0.3\_1000 b) M0.3\_1700 c) M0.5\_1000 d) M0.3\_1000t..... 38

Figure 31- XRD diffractograms of heat treated multilayer ML\_60 film: conventional XRD on the left and synchrotron energy XRD on the right. .... 39

Figure 32- DSC curves of heat treated films: a) M0.3\_1000, b) M0.3\_1700, c) M0.3\_1000t, d) ML\_4, e) ML\_60..... 40

Figure 33- DSC curve of M0.5\_1000 heat treated film. .... 41

Figure 34- Hardness of as-deposited and heat treated (400°C) monolithic films..... 43

Figure 35- Hardness of as-deposited and heat treated (400°C and 500°C) multilayer films. .... 43

Figure 36- Indentation curves of the as-deposited and heat treated (400 and 500°C) ML\_60 film. .... 44

Figure 37- Scheme relating nanoindentation microstructural mechanisms with material hardness, energy dissipation and energy recovery for NiTi shape memory alloys [61]. .... 45



**LIST OF TABLES**

Table 1- Different target layouts used for producing NiTi films by sputtering*.....	9
Table 2- Deposition parameters for the monolithic films.....	22
Table 3- Deposition parameters for the multilayer films. ....	22
Table 4- As-deposited films' chemical composition.....	29
Table 5- Mechanical behavior of as-deposited films.....	42
Table 6- Mechanical behavior of heat treated films. ....	42



## LIST OF SIMBOLS

### List of Symbols

A-Austenite phase

$A_f$ -Austenite phase final temperature

$A_s$ -Austenite phase start temperature

Ar-Argon

E-Young's modulus

$E_r$ -Reduced Young's modulus

$M_f$ -Martensite phase final temperature

$M_s$ -Martensite phase start temperature

Ni-Nickel

R-R phase

$R_f$ -R phase final temperature

$R_s$ -R phase start temperature

Si-Silicon

T-Temperature

Ti-Titanium

$T_m$ -Melting temperature

V-Vanadium

$d$ -Interplanar spacing of the crystal, parameter used in Bragg's Law

$n$ -Integer number, parameter used in Bragg's Law

$\lambda$ -Wavelength of x-rays, parameter used in Bragg's Law

$\nu$ -Poisson coefficient

$\theta$ -Angle of reflection, parameter used in Bragg's Law

$\delta$ -Nickel-rich precipitates

## Acronyms/Abbreviations

DEM-Departamento de Engenharia Mecânica (Portuguese for Mechanical Engineering Department)

DESY-Deutsches Elektronen Synchrotron (German Electron Synchrotron)

EDS-Energy Dispersive X-Ray Spectroscopy

HiPIMS-High Power Impulse Magnetron Sputtering

ICDD-International Centre for Diffraction Data

IPN-Instituto Pedro Nunes (Portuguese for Pedro Nunes Institute)

M-Monolithic

Me-Metal

MEMS-Microelectromechanical Systems

ML-Multilayer

SE-Superelasticity Effect

SEM-Scanning Electron Microscopy

SMA-Shape Memory Alloy

SME-Shape Memory Effect

SR-Synchrotron Radiation

TEM-Transmission Electron Microscopy

XRD-X-Ray Diffraction

## 1. INTRODUCTION

The accelerating technology development over the last decades has been replacing single macro devices with compact micro solutions: compound and complex systems with microscopic devices incorporating both electronic and moving parts called microelectromechanical systems (MEMS). This relentless hunger of industry calls for never ending mechanical and functional solutions enabled by science knowledge. In this context, Shape Memory Alloys (SMA) are studied to investigate their appeal and distinction in this field.

SMA's have exceptional functional properties: shape memory effect (SME) and superelasticity effect (SE). Exposing these materials to a controlled external stimulus such as stress or temperature change can cause a unique response. For the superelasticity effect, this response is an abnormal material elongation before plastic deformation, while for the shape memory effect, the response is a complete material recovery to an initial form when heated above austenitic temperature. The presence of these distinctive effects is tied to a fine combination between material's processing and chemical composition. In fact, minimal deviations in chemical composition cause major differences in material morphology and composition, which will greatly impact final results.

The Shape Memory Alloy chosen is NiTi. This compound reveals superior characteristics and has been rising interest and popularity in the last decades in the sensor and actuator industry. In this dissertation, both near equiatomic and highly Ni-rich NiTi are studied, with the later being the subject of scarce research in the available literature. With the intention of applying these materials in MEMS, it was decided to work with materials in the form of films. From a wide range of available techniques, it is consensual that the sputtering technique has many advantages in successfully producing films. For that reason, magnetron sputtering is the chosen technique to deposit the films to be studied.

Two strategies were adopted to prepare NiTi-based films: i) sputtering from a single NiTi target, ii) sputtering from two separate targets (Ni and Ti). In both cases, to obtain the desired NiTi intermetallic it was necessary to heat treat the films. In addition, some deposition parameters were varied, to study their influence on the films' properties. For this purpose, several characterization techniques were used: Profilometry for measuring

thickness, Energy Dispersive X-ray Spectroscopy to determine chemical composition, Scanning Electron Microscopy to study the morphology, X-Ray Diffraction for phase investigation, Differential Scanning Calorimetry for thermophysical analysis, and finally Nanoindentation to evaluate the films' mechanical properties.

With all these data in hand, it should be possible to produce and improve the properties of NiTi-based films that could be promising and possibly open doors in MEMS field.

The present dissertation is organized in five Chapters, being the first the Introduction chapter. The second chapter is the State of Art, where the literature's most relevant information is compiled. The third chapter exhibits a collection of the materials, equipment and characterization techniques used, including the procedures to enable the reader to reproduce each process. In the fourth chapter the results are presented, analyzed, and discussed which lead to the conclusions and future works of the fifth chapter.

## 2. STATE OF ART

### 2.1. Shape Memory Alloys

Shape memory alloys (SMAs) belong to the class of advanced materials with unique functional properties such as shape memory effect (SME) and superelasticity effect (SE). These alloys present excellent mechanical properties, a very high resistance to corrosion [1] and biocompatibility [2], which allow these materials to be used in a wide range of applications.

When subjected to an external stimulus, SMAs can undergo a phase change that is the key factor for the existence of SMEs and SE. This phase transformation is classified as thermoelastic martensitic transformation, which is characterized by the reversible transformation between the austenite phase (A), stable at temperatures higher than the austenitic finish transformation temperature ( $T > A_f$ ); and the martensitic phase (M), stable at temperatures lower than the martensitic finish transformation temperature ( $T < M_f$ ) [3,4].

SMAs are typically composed by a combination of metallic elements such as titanium, nickel, copper, magnesium, zirconia, among other, being NiTi (nickel and titanium) the most famous SMA alloy, and the one that will be explored in this study.

### 2.2. NiTi Shape Memory Alloys

#### 2.2.1. NiTi Film Composition

The control of the chemical composition of the films is crucial since the shape memory effect or superelasticity depend on the Ni content of the shape memory alloy.

Slight variations in the Ni content can result in materials with other intermetallic phase besides NiTi, particularly for the Ni-rich side of the phase diagram (Figure 1).

Single crystal NiTi usually have low critical stress for slip. As superelasticity only occurs when austenite phase is present, which is at temperatures above  $A_s$ , it is very hard for this effect to be present (See example “B” in Figure 2 and its very narrow superelasticity zone). However, for aged Ni-rich NiTi alloys “the critical stress for slip is strengthened by precipitation hardening” [1], creating room for stress at temperatures higher than  $A_s$ , without

incurring the possibility of plastic deformation. (See example “A” in Figure 2 and its very wide superelasticity zone).

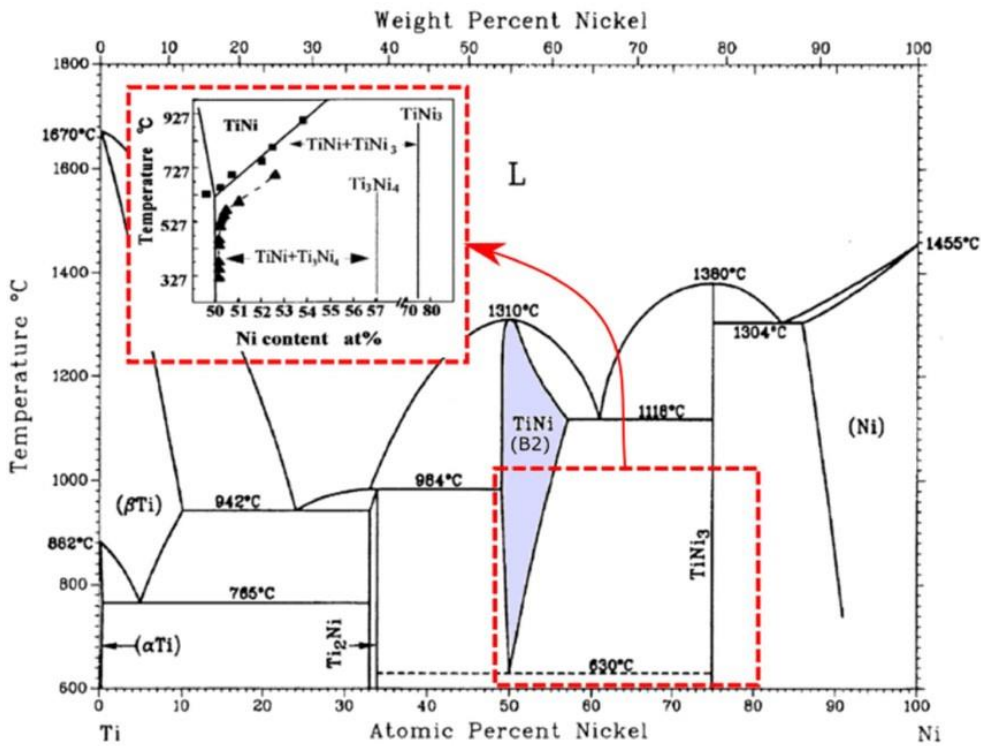


Figure 1- Ni-Ti phase diagram with emphasis on Ni-rich lower temperature section [5].

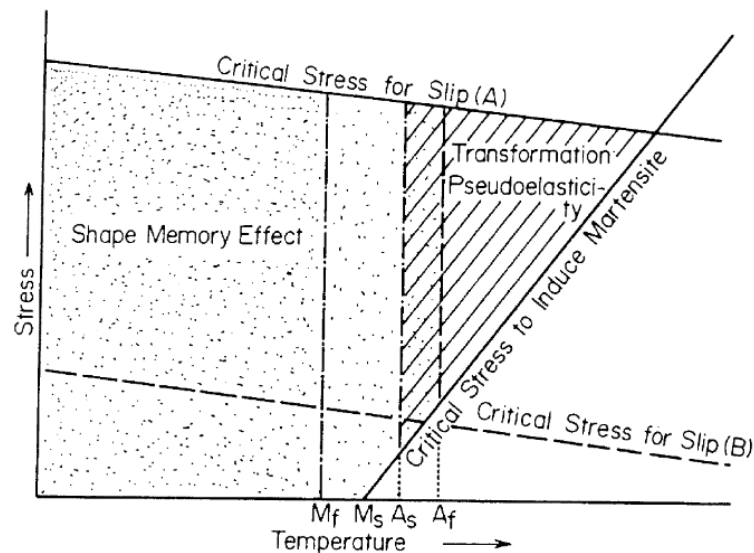


Figure 2- Representation for the appearance of superelasticity and shape memory effect [1].

As it can be observed in Figure 3, martensite start temperature will greatly decrease



with minimum atomic Ni (nickel) % variation, being the variation from equiatomic film to 51% Ni enough to almost halve transformation temperature [6].

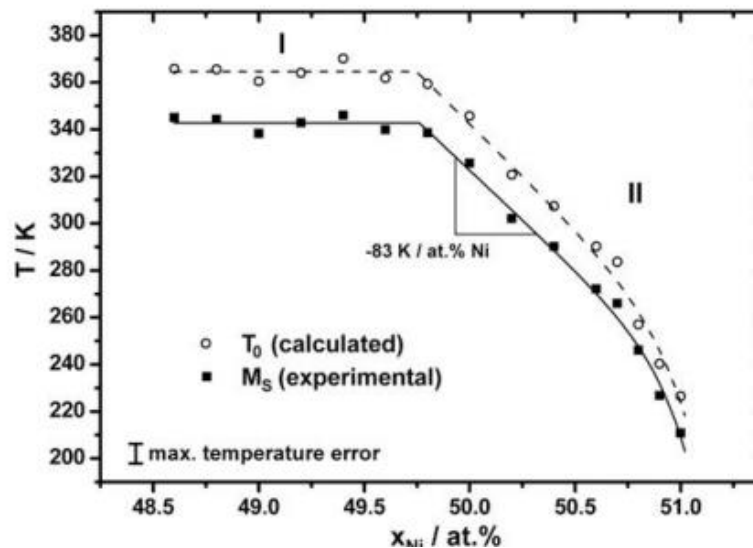


Figure 3- Influence of the nominal Ni concentration on the measured  $M_s$  temperature and calculated  $T_0$  temperature (calculated according to Tong and Wayman for a given film [6]).

Shape memory effect is possible if the working temperature of the alloy is lower than  $M_f$  temperature. If  $M_s$  temperature decreases too much, so does  $M_f$  temperature and shape memory effect would only be achievable in sub-zero room temperatures. This way, Ti-rich NiTi alloys are a must to obtain  $M_s$  temperatures as high as  $70^\circ\text{C}$ , temperatures which are easily achievable in the majority of the applications, allowing these alloys to have shape memory effect.

### 2.2.2. Shape Memory Effect

Shape memory effect is this alloy's most known ability: the ability to return to the original form after being strained, through heating.

To better understand how memory effect works, Figure 4 can be analyzed.

At working temperature ( $T > M_f$ ), the alloy starts in the twinned martensitic phase (Point O).

As the alloy is loaded, its crystal configuration will accommodate the stress by stretching (Point P). This stretch doesn't disappear once the alloy is unloaded (Point Q).

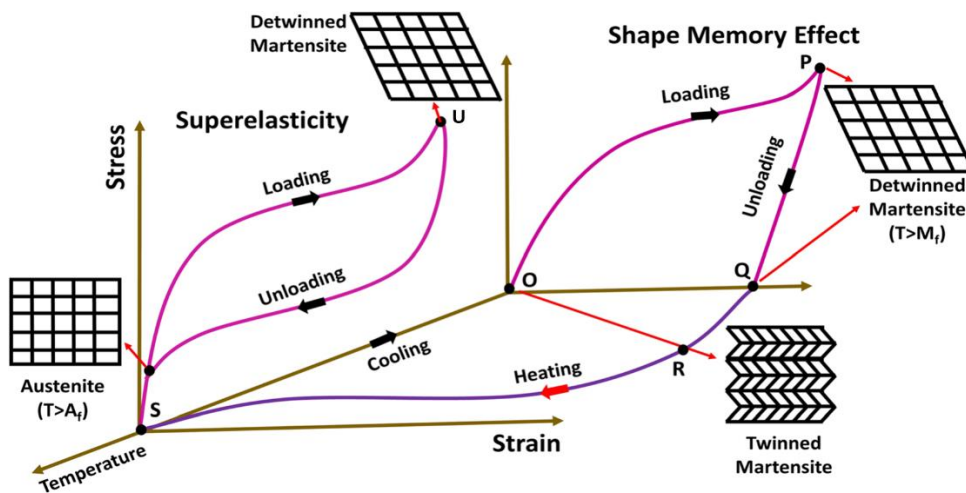


Figure 4- Crystal transformations in Superelasticity Effect (left) and Memory Shape Effect (right) [7].

The alloy is then heated, promoting a change back to austenite phase, and the macrostructure back to the original form (Point S).

After cooling, the macrostructure remains the same as phase changes back to twinned martensite, closing the cycle. (Point O).

An example of this effect is evident in Figure 5, where a deformed NiTi paper clip returns to the original form with the stimulus of heated water.

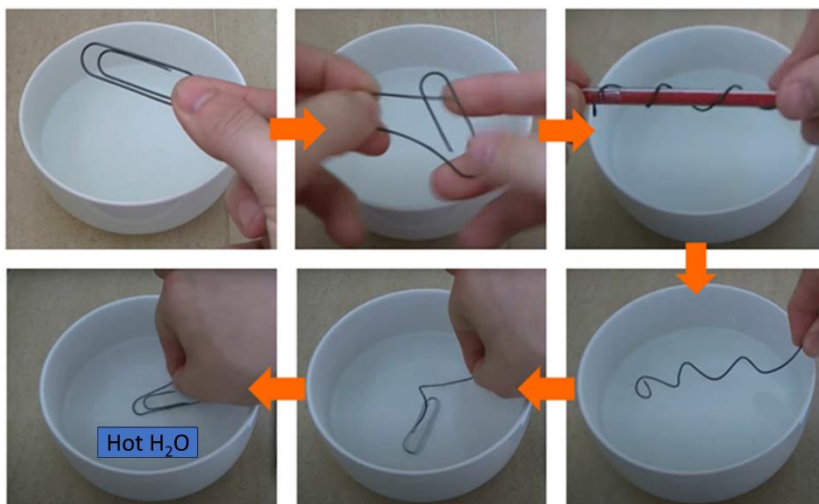


Figure 5- Paper Clip made of a SMA showing the Shape Memory Effect [8].

### 2.2.3. Superelasticity Effect

Superelasticity effect is the ability to return to the original form after complete removal of the stress applied. This occurs when the alloy is in the austenitic field, which means it is above austenite finish temperature ( $A_f$ ) [9].

In Figure 4, the superelasticity effect is shown. While unloaded, the alloy is in austenitic field (Point S), then a force is applied and there is a change to detwinned martensite phase (Point U). When the force is relieved, there is a change back to the original phase, combined with a return to the original form.

A utility of this effect is, for example, glasses temples made of NiTi, which can be highly deformed and return to the original form without plastic deformation (Figure 6).



Figure 6- Glasses made of a SMA showing the superelasticity effect.

### 2.2.4. Ni-Rich NiTi Alloys

NiTi alloys have several possible compositions, being the Ni-rich NiTi an interesting iteration. This variant can be called 60NiTi because it is characterized by nickel weight percentages ranging from 55 to 60 wt.% [10,11,12,13,14].

In equiatomic and Ti-rich NiTi there are virtues such as superelasticity and the memory shape effect, which make them usable in a wide range of applications such as actuators and arch wires. However, these variants lack dimensional and microstructural stability, and are soft when compared to 60NiTi [10,14].

As stated in section 2.2.1, NiTi films with high Ni composition will have negative  $M_s$  and  $M_f$  temperatures, and consequently, low  $A_s$  and  $A_f$  temperatures as well. These films will benefit the best from the superelasticity effect, because they are austenitic stable in a wide range of temperatures: temperatures higher than  $A_f$  temperature, which includes room temperature.

This last fact combined with the high dimensional and microstructural stability [10,14], high hardness [10,14], low density [11,12], low elastic modulus [10,11] and superelasticity (making them highly resistant to excessive shock loads [11]) ensure 60NiTi's suitability in structural applications [10], tool manufacturing [10,11], gears and bearing applications [10,11,12], as well as highly innovative areas such as aerospace, marine and automotive engineering, intelligence control, medical applications, etc. [10,13].

### **2.3. NiTi Thin Films**

The use of NiTi films instead of bulk alloys results in faster cooling rates (because of the higher surface/volume ratio) allowing SMA use for applications in smaller components with better efficiencies [4].

Among deposition techniques such as pulsed laser deposition, electron beam evaporation, ion beam deposition, plasma spray technique, ion plating, and flash evaporation; magnetron sputtering has proved to be the most successful and most widely used technique to prepare NiTi-based thin films [7].

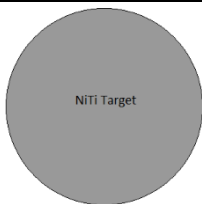
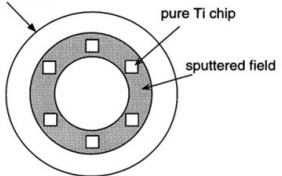
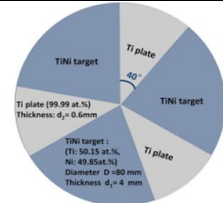
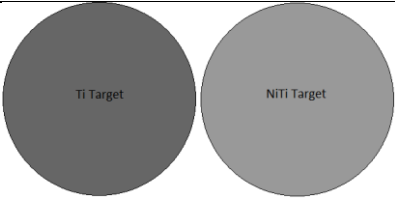
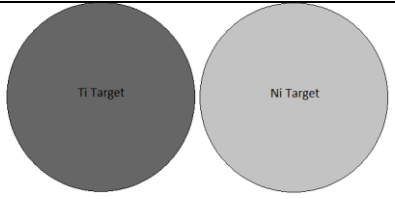
Sputtering is a physical vapor deposition technique. It works by applying a high-voltage electric field on a target, accelerating ions towards the target, and ejecting its atoms that will eventually collide with the substrate, creating a film. For that, an inert gas is used, usually Argon because it has a good compromise between ion size and cost. Low Ar gas pressures (<0.05 Pa) conduct to high energy atoms reaching the substrate, leading to atomic peening which causes increasing compressive stresses in the film. Intermediate pressures (from 0.05 Pa to 0.5 Pa) create rather dense films with few defects. Films produced with higher Argon pressures (>1 Pa) will be subjected to less peening effect, which means the film will be less dense, more brittle, more porous and with columnar morphology [7,15,16].

Magnetron sputtering is a sputtering variant that uses a magnetic field to enhance target sputtering yield, in other words, the number of atoms ejected. The potential disadvantages of this technique are the preferential erosion of the target where the magnetic

field is the strongest [3], and the interference of the magnetic field with ferromagnetic alloys such as Ni. To solve this last problem, the use of Ni targets with a few percent of Vanadium is reported in the literature [17]. The addition of V cancels the target ferromagnetic properties.

There are multiple ways to obtain NiTi films by magnetron sputtering, as shown on Table 1. The conventional approach is the use of a single NiTi alloy target. In this case, due to the higher sputtering yield of Ni compared to Ti, the films tend to have Ni-rich chemical compositions (2 to 4 at% richer than the target [7]). To control the Ni percentages, variants such as the NiTi alloy target with Ti plates or the NiTi alloy target with a second Ti target are used. In addition, the usage of separate Ni and Ti targets is also possible. In this case, after deposition a multilayer film is obtained.

**Table 1- Different target layouts used for producing NiTi films by sputtering\*.**

Targets	Layout	Ref.
NiTi		[18,19,20]
NiTi+Ti	<div style="display: flex; align-items: center;"> <div style="text-align: center;"> <p>Ti-50at%Ni alloy target</p>  </div> <div style="margin: 0 10px;">OR</div> <div style="text-align: center;">  </div> </div>	[21,22]
NiTi/Ti		[2,3]
Ni/Ti multilayers		[3,4,15,23,24,25,26]

\* To simplify, all targets were drawn as circles

The multilayer films approach means that the as-deposited films are composed of alternated layers Ni- and Ti-rich, whose single layer thicknesses depend on the substrate rotation speed. The higher the rotation speed, the lower the multilayer period (bilayer thickness). This variant is more flexible, when it comes to control the average chemical composition, which can be achieved by simply adjusting the power applied to each target. Furthermore, it has additional advantages, such as denser films, less residual stress than its counterparts, and grain size control [7,21]. The grain size is limited by the individual layer thickness; thus, it increases as the period increases. To control the grain size, the modulation period can be varied by changing the substrate rotation speed [4]. If the total thickness is known, the modulation period can be estimated using Equation (1):

$$period (\lambda) = \frac{total\ thickness}{deposition\ time * rotation\ speed} \quad (1)$$

Shape memory effect or superelasticity effect can only be achieved if the alloy has martensite or austenite phase present, which means that in the case of multilayer films, Ni and Ti must react to form the NiTi intermetallic phase.

In the case of monolithic films prepared using a NiTi alloy target, the as-deposited films tend to be amorphous [19,20]. Therefore, the equilibrium austenitic phase can only be achieved after crystallization, which is possible either by depositing the films at high substrate temperatures [19], or by post-annealing treatment [20].

John A. Thornton [16] succeeded on relating deposition substrate temperature and deposition argon pressure with the film's surface and cross-section microstructure (Figure 7). For reference, 1mTorr is equal to about 0.133 Pa.

The deposition temperature also has impact on the final film's phasic composition produced using an alloy target (monolithic films) or by co-sputtering from separated targets (multilayer films). When the monolithic films are deposited with substrate temperatures around 425°C, the NiTi peak becomes evident in the X-ray diffraction (XRD) diffractograms [2,19]. Using high power impulse magnetron sputtering (HiPIMS), X. Bai et al. [22] obtained in-situ crystalline NiTi thin films at a low substrate temperature (230°C). Although less usual, it is possible to use separate targets and heat the substrates during the deposition to obtain in-situ crystalline NiTi films [26]. In this case, the reported substrate temperature is 450°C.

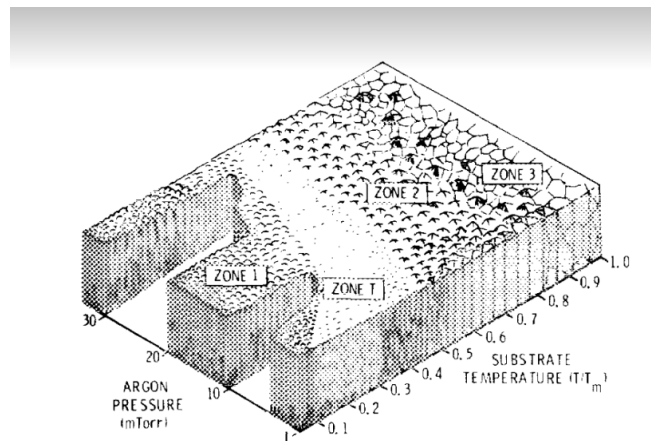


**Figure 7- Microstructure zone diagram for metal films deposited by magnetron sputtering where  $T_m$  is the coating material melting point and  $T$  is the substrate temperature [16].**

In alternative, whatever the sputtering approach, the deposition stage can be separated from the heat treatment stage.

In multilayer films, post heat treatments at temperatures above 400°C are the most used to crystallize NiTi [3,15,23]. As an example, in Figure 8 several diffractograms of equiatomic Ni/Ti multilayer films with different modulation periods are shown at different annealing temperatures. It is evident that the higher the period of the multilayer film, the lower the temperature for the austenitic NiTi (110) XRD peak to be indexed. This temperature ranges from 375°C ( $\Lambda = 70$  nm) to 450°C ( $\Lambda = 5$  nm) [4].

In-situ transmission electron microscopy (TEM) together with electron diffraction, allowed to observe the appearance of NiTi grains after 6 min at 400°C [27].

Typically, the monolithic films are post-annealed at temperatures above 500°C [22]. For near equiatomic monolithic films, temperatures of 600°C were used to obtain well defined NiTi XRD peaks [18,20]. Annealing temperature is critical since a low temperature might not be enough to fully crystallize the films. On the other hand, a temperature higher than necessary can promote the precipitation of undesired phases such as NiTi<sub>2</sub>, Ni<sub>3</sub>Ti, and oxides, that can influence the films' mechanical properties as well as the phase transformation temperatures [7,20].

For both, monolithic and multilayer films, the study of the hardness and Young's modulus is important to characterize the shape memory thin films. These mechanical properties can be evaluated by depth sensing indentation [28]. If conventional indentation is to be used in thin films, the indentation depth would be too high taking in consideration the

reduced thickness of the films and the mechanical properties would be significantly influenced by the substrate. According to the literature, a maximum indentation depth close to 10% of the films' total thickness should avoid the influence of the substrate on the hardness measurements [29,30]. However, regarding the Young's modulus the influence of the substrate can be noticed even for indentation depths of this magnitude. In this context, nanoindentation is the preferred technique since it can work with very low loads and depths.

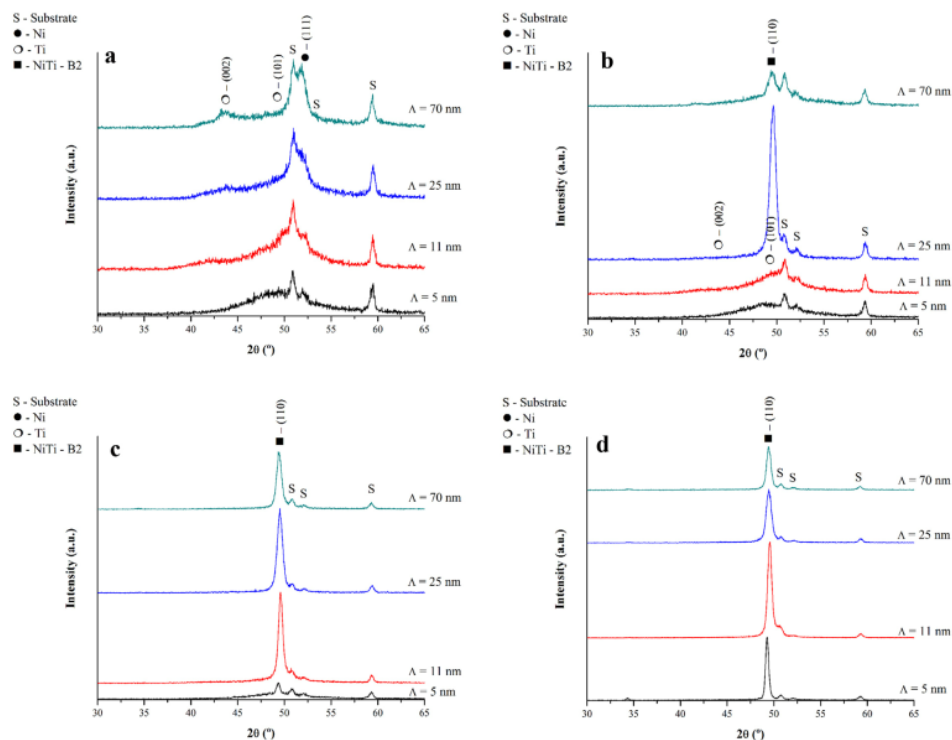


**Figure 8- XRD diffractograms for Ni/Ti multilayer thin films with different periods at a) 300, b) 375, c) 400 and d) 450 °C. Substrate diffraction peaks are labelled with "S" [4].**

When comparing monolithic with multilayer films, it is expected for the later to be harder, because the multilayer design has inherently more interfaces which contribute to increase the hardness [31,32]. In fact, the hardness of Me1/Me2 (Me – metal) multilayer films is higher than the value that results from a simple rule of mixtures based on Me1 and Me2 films' hardness [32]. The modulation period of Me1/Me2 multilayer films influences the hardness. In general, the hardness increases as the period decreases. However, for short periods, in certain Me1-Me2 systems, after achieving a maximum value there is a hardness decrease as the period decreases further (Figure 9) [33].



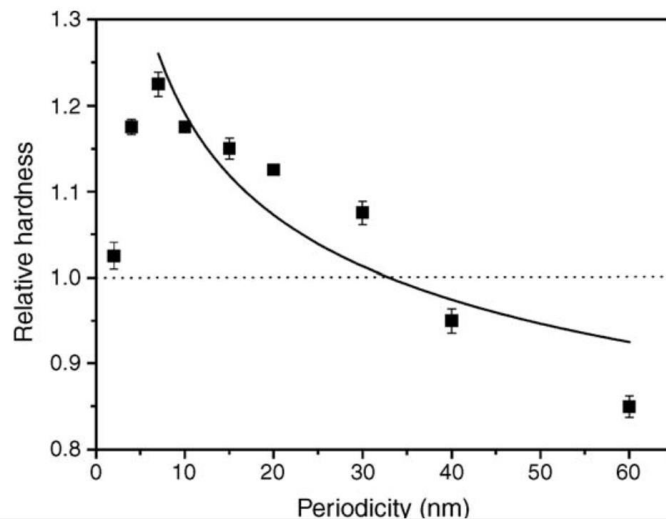


Figure 9- Hardness of Ag/Co multilayer films as a function of the period [33].

## 2.4. Applications

Taking advantage of the shape memory alloys' peculiar characteristics, several applications can be envisaged. In fact, there are numerous applications for which NiTi-based SMAs are potential candidates.

A first example would be the use of NiTi SMAs in endodontic instruments such as drills (Figure 10). Compared to conventional materials, the use of this alloy creates safer and more effective rotary instruments with dynamic properties that can better sustain flexural and torsional stresses [34].



Figure 10- Rotary endodontic instruments [34].

NiTi can also be used in orthodontic treatment, mainly for the alignment of the teeth. This orthodontic treatment consists in applying a continuous but low force to a tooth, moving it through the alveolar bone of the jaws without causing any permanent damage [35]. This procedure uses arch wires to create the needed tension in the teeth (Figure 11). The arch wires have very specific property requirements: biocompatibility, high modulus of resilience, stiffness, formability and springback, which are properties where a superelastic NiTi alloy excels [35].



**Figure 11- NiTi arch wires.**

Still in the biomedical field, porous NiTi alloys are being developed to replicate bones' mechanical properties, such as the low elastic modulus. Nonetheless, porosity will negatively impact compressive stress strength, superelastic strain and biocompatibility which makes the balance a challenge [36]. Figure 12 shows some examples of the use of porous NiTi as implants to replace bones in the human body.

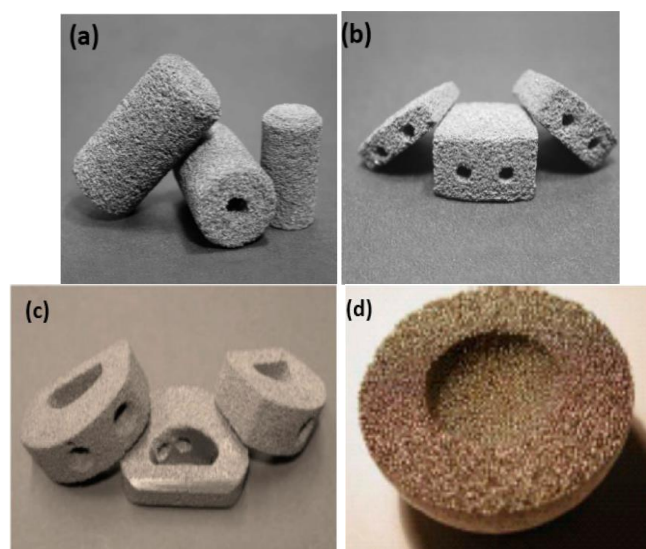


**Figure 12- (a) Cervical spine implantation; (b) lumbar spine implantation; (c) intervertebral fusion device and (d) acetabular cup (hip implant) [36].**

NiTi SMAs are also very useful in engineering applications. Their high strain range and spontaneous strain recovery can be used in self-centering earthquake resisting structural systems [37]. There are also some NiTi solutions for creating earthquake proof bridges [38], as observable in Figure 13.

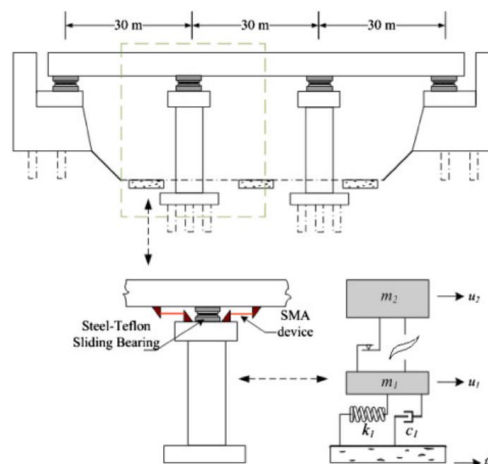


Figure 13- Model of an earthquake proof bridge that uses NiTi alloy materials [38].

One branch of equipment with rising interest is the microelectromechanical systems (MEMS). These systems require working sensors and actuators at the microscopical level. NiTi SMAs are active materials that can already be downsized, thus can have significant impact in the development of MEMS. This alloy's electrical resistance varies with both stress and strain, allowing the creation of sensors using controlled voltages on NiTi wires, being possible to measure the displacements of moving parts (Figure 14) [39,40].

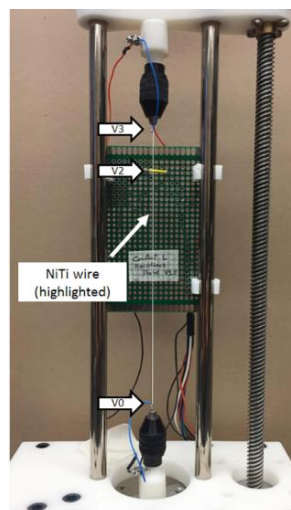


Figure 14- Displacement measurement testing on a NiTi wire [40]

In the actuator perspective, the possibilities are endless. By controlling the alloy’s temperature, martensite transformation can be promoted. As a result, the position of the material can change, and motion or force can be induced at the microscopic level.

Microvalves and micropumps to control microfluidic systems using a moving diaphragm have already been developed (Figure 15) [41,42]. Microgrippers using a wire with different transformation temperatures at each length are shown in Figure 16 [43]. In addition, microswitches, microspacers, microwrappers, microrobots, among other, have been reported in the literature [7,44].

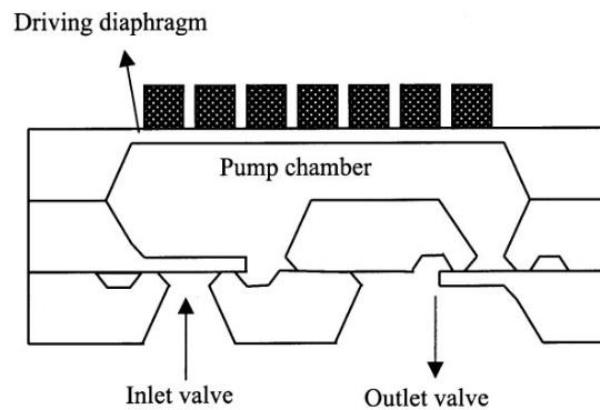


Figure 15- Schematic of a micropump and the corresponding NiTi/silicon driving diaphragm [42].

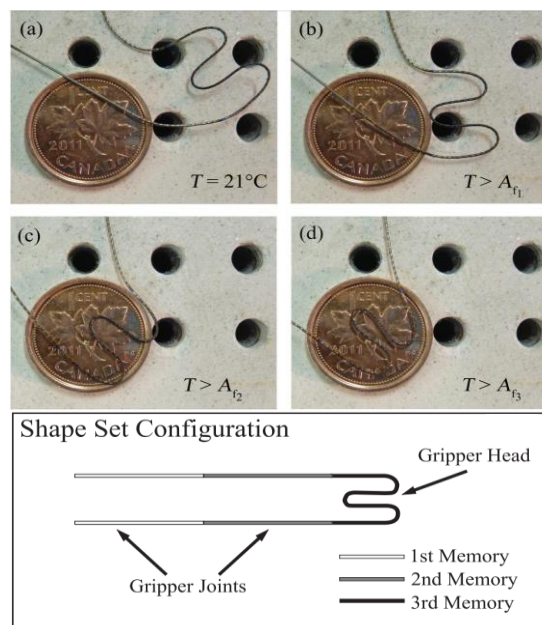


Figure 16- (a-d) Photographs of the different stages of activation of the microgripper (upper images) and wire’s shape set configuration (lower image) [43].

In this context, an interesting mechanism was designed by Yang X et al [45], where a robot was built with catalytic artificial NiTi-Pt wires as muscles. Once fed with a combustible such as methanol (stored within the robot), the wire gets excited by the heat of the reaction, triggering the moving parts (Figure 17).

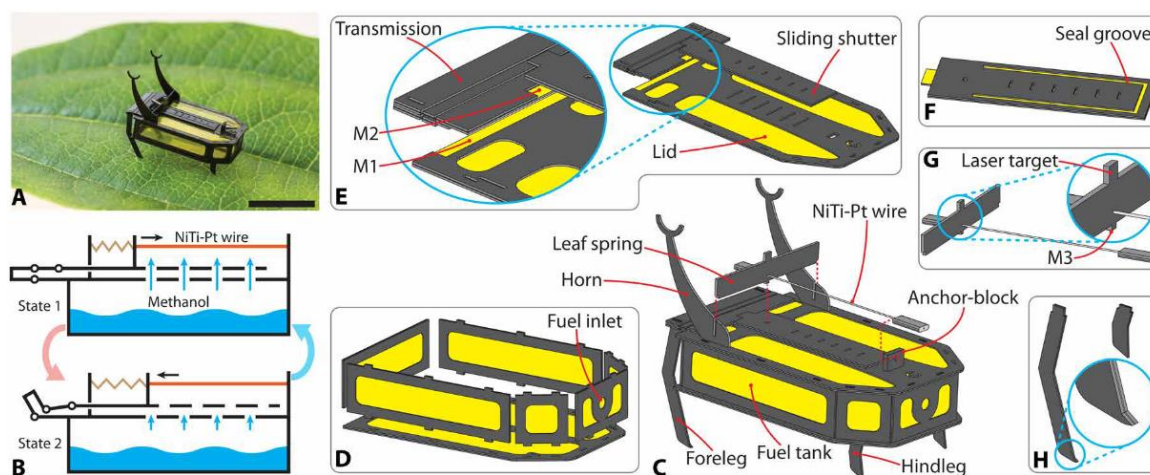


Figure 17- RoBeetle and corresponding schematics and detailed views [45].



## **3. MATERIALS AND METHODS**

### **3.1. Materials**

#### **3.1.1. Substrates**

Substrates are the materials on which the atoms of the deposition accumulate to create the film. For this thesis, monocrystalline silicon substrates were used. The silicon wafers from which the substrates were cut were mirror finished in one of the sides. Before deposition, the Si substrates were subjected to ultrasound cleaning, in acetone and alcohol baths, for 5 minutes each. After exiting the ultrasound machine, the substrates are dried with hot air.

To measure the thickness of the films by profilometry, a drop of boron nitride is placed on one of the substrates in each batch.

#### **3.1.2. Substrate Holders**

Substrate holders are the materials on which the substrates are fixed onto using silver glue. Copper substrate holders were used, to take advantage of Cu high thermal conductivity which allows heat dissipation during the deposition process, avoiding high substrates' temperatures.

#### **3.1.3. Targets**

Targets are the materials from which the atoms of the deposition are detached. In this thesis 3 types of targets (150 mm x 150 mm x 5-7 mm) were used: NiTi (99,9 % pure), titanium (99,99 % pure) and nickel (99,99 % pure). A near-equiatomic NiTi target (Ti-49.9 at.% Ni) was used to produce monolithic films, while the Ti and Ni targets were used to prepare multilayer films with nanometric periods. The Ni target contains 7 wt.% of vanadium, so that it becomes nonmagnetic [17].

## 3.2. Methods

### 3.2.1. Deposition Technique

As often used to obtain thin films, the deposition technique in this thesis was magnetron sputtering.

Sputtering is a physical vapor deposition technique, where the targets and substrates are inside a vacuum chamber with the presence of an inert gas; being argon the most commonly used because it has a good compromise between ion size and cost.

For this technique to work, a high-voltage electric field is applied on each target, ionizing the inert gas and creating plasma. This electric field accelerates argon ions ( $\text{Ar}^+$ ) towards the target(s) (cathode). When the ions collide with the target, some of its atoms are ejected (by effect of exchange of momentum) and will travel towards the substrates creating a film. The whole process occurs inside a vacuum chamber to minimize the gases present in the atmosphere that would oxidize and contaminate the substrates.

When the magnetron sputtering variant is used, the plasma concentrates near the targets which generates a more efficient deposition. To be noted that the targets will have a less uniform wear, which will require a higher attention.

### 3.2.2. Deposition Equipment

The equipment used for the magnetron sputtering deposition is from a German company called Hartec (Figure 18).

The deposition chamber has an ion beam and two distance adjustable targets, each with its magnets. Therefore, it is possible to deposit multilayer films. The equipment has four different power supplies; two used for the targets, one to polarize the substrate holder and one for the ion beam. The vacuum system is composed of two pumps: the primary, which is responsible for creating vacuum from the atmospheric pressure down to approximately 30-40 Pa, and the secondary pump (turbomolecular), which aided by the primary pump can reach pressures in the range of  $10^{-4}$  Pa.



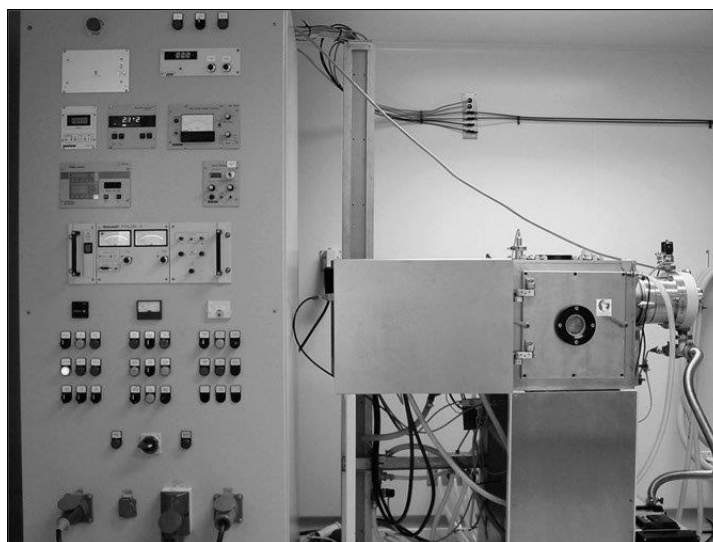


Figure 18- Deposition equipment Hartec of DEM.

### 3.2.3. Deposition Conditions

Prior to the deposition itself, it is necessary to create the needed vacuum, before introducing the argon and cleaning the substrates by ion bombardment (etching).

Pressures of around  $4 \times 10^{-1}$  mbar (40 Pa) were achieved through the primary pump, while lower pressures were reached with the help of the secondary pump. After attaining the desired vacuum level, a heating and etching procedure is done with an argon pressure of  $1.5 \times 10^{-3}$  mbar (0.15 Pa). The objective is to remove impurities at the substrates surface. To start the deposition process, Ar is introduced up to the desired pressure is attained, and then the target(s) power supplies are turned on.

The monolithic films deposited in this work are summarized in Table 2, while the multilayer films are presented in Table 3. The nomenclature followed is M\_pressure[Pa]\_power[W] for the monolithic films, and ML\_modulation.period[nm] for the multilayer films. According to the total thickness of the multilayer films and substrates' rotation speed, the estimated periods are close to 4 and 60 nm for the ML\_4 and ML\_60 films, respectively.

**Table 2- Deposition parameters for the monolithic films.**

Film	Target(s)	Distance <sup>1</sup> [mm]	Pressure [Pa]	Specific Power [Wmm <sup>-2</sup> ]	Dep* Time [min]	Rot* Speed [rpm]	Thickness [μm]
M0.3_1000	NiTi	75	0.3	4.44x10 <sup>-2</sup> (1000 W)	60	23	3.2
M0.3_1700	NiTi	75	0.3	7.56x10 <sup>-2</sup> (1700 W)	28	23	2.7
M0.5_1000	NiTi	75	0.5	4.44x10 <sup>-2</sup> (1000 W)	60	23	3.4
M0.3_1000t	NiTi	75	0.3	4.44x10 <sup>-2</sup> (1000 W)	120	23	5.1

\* Dep and Rot are abbreviations of Deposition and Rotation, respectively.

**Table 3- Deposition parameters for the multilayer films.**

Film	Target(s)	Distance [mm]	Pressure [Pa]	Specific Power [Wmm <sup>-2</sup> ]	Dep Time [min]	Rot Speed [rpm]	Thickness [μm]
ML_4	Ti Ni	Ti: 75 Ni: 95	0.4	Ti: 7.42x10 <sup>-2</sup> Ni: 2.76x10 <sup>-2</sup>	30	23	2.5
ML_60	Ti Ni	Ti: 75 Ni: 95	0.4	Ti: 7.42x10 <sup>-2</sup> Ni: 2.76x10 <sup>-2</sup>	32	1.5	3.0

### 3.2.4. Post Deposition Treatments

To achieve superelasticity or shape memory effect, NiTi phase must be present. As the substrates were not heated, it was not expected that NiTi formed, and a heat treatment is needed to obtain the intermetallic phase [20]. As such, all films were heat treated at 400°C for 1h in a horizontal oven present in DEM. The multilayer film with the highest period was also heat treated at 500°C during 1h.

To perform the heat treatments, the samples were put in an alumina crucible, and placed in the oven's quartz tube. After achieving a vacuum pressure of around 2x10<sup>-4</sup> mbar (0.02 Pa), hydrogenated argon was introduced in the oven until a pressure of 5x10<sup>-3</sup> mbar (0.5 Pa) is reached. Afterwards, the heating up to the desired temperature was carried out at 20°C/min. Once attained the predefined temperature, it was maintained during 1 h, after which the oven was switched off, and the samples were let to cool inside the oven.

<sup>1</sup> Target to substrate distance

### **3.2.5. Characterization Techniques**

#### **3.2.5.1. Profilometry**

In the context of the NiTi films under study, profilometry was used as an easy way to measure the total film thickness immediately after the depositions. For this purpose, prior to the deposition, a drop of boron nitride was placed onto the Si substrate, as mentioned. After the deposition, the drop was removed in alcohol ultrasound bath, allowing the thickness to be measured through the height of the profile's degree created by the absence of the drop.

#### **3.2.5.2. Scanning Electron Microscopy (SEM)**

Scanning Electron Microscopy (SEM) is a physical technique used to visualize and analyze the surface and/or cross-section morphology of a material at high resolution.

SEM works by emitting a focused beam of electrons onto the material under study, followed by the analysis of the response-signals emitted by the material. These signals include secondary electrons, backscattered electrons and X-rays.

Secondary electrons are used mainly to exhibit the material's topography map, while backscattered electrons are used to reveal compositional variations in the sample: heavy elements usually are shown as brighter, while light elements are shown as darker areas in SEM images.

Emitted X-rays are linked to the Energy Dispersive X-ray Spectroscopy (EDS) analysis, because each chemical element emits its own characteristic X-rays at a specific energy. Therefore, SEM/EDS is a semi-quantitative mode to obtain the chemical composition of the films under study.

The equipment used in this thesis is a field-emission gun Zeiss Merlin SEM microscope equipped with EDS present at Instituto Pedro Nunes (IPN) (Figure 19). Accelerating voltages of 2 and 10 kV were used for imaging and EDS, respectively.



Figure 19- IPN SEM equipment.

### 3.2.5.3. X-ray Diffraction (XRD)

X-ray Diffraction (XRD) is a very powerful technique that uses X-rays to study the structural characteristics of the materials, such as the identification of the present phases and their crystal structure.

In the context of this thesis, XRD allowed the analysis of the as-deposited films' present crystalline phases, if any, and more importantly, the analysis of the heat treated films' phases. This is a must to ensure the purpose of this thesis, namely the study of the deposition parameters and their influence in achieving austenitic superelastic NiTi films.

X-ray Diffraction works by emitting X-rays which will diffract when in contact with the crystalline sample. XRD works based on Bragg's law principle (Equation (2)) which relates the wavelength of the incident x-rays, the angle of incidence and the spacing between the crystal lattice planes of atoms [46].

$$n\lambda = 2d \sin(\theta) \quad (2)$$

Where:  $n$  is an integer number,  $\lambda$  is the wavelength of x-rays,  $d$  is the interplanar spacing of the crystal and  $\theta$  is the angle of reflection.

For the XRD measurement, the identification of the diffraction peaks was performed based on the ICDD<sup>2</sup> database.

---

<sup>2</sup> International Centre for Diffraction Data

The XRD tests were run in 2 different systems (lab source and synchrotron radiation) that are described in the following sections.

#### 3.2.5.3.1. Conventional X-Ray Source (XRD)

The conventional X-ray source can also be called a reflection XRD.

In this study, the equipment used was XPert Pro from PANalytical coupled with a PW 3020/00 goniometer (IPN, Coimbra), with current and voltage of 35 mA and 40 kV respectively, using  $\text{CuK}\alpha$  radiation.

#### 3.2.5.3.2. Synchrotron Radiation X-ray Diffraction (SR-XRD)

The Synchrotron Radiation X-ray Diffraction can also be called a transmission X-ray diffraction. This type of XRD uses very high energies, fact that ensures full sample penetration, guarantees a higher precision and resolution, and consequently increases the visibility of phases that are present in very low percentages. Furthermore, this variant has exceptionally fast read times which allows in-situ analysis that are not possible with the conventional method. Synchrotron radiation comes from particle accelerators, with high cost and as such restricted access.

The structural characterization using synchrotron radiation was performed in beamline P07 High-Energy Materials Science (HEMS) of Petra III/DESY (Deutsches Elektronen-Synchrotron), located at Hamburg, Germany (Figure 20). The measurements used a wavelength of  $0.1467 \text{ \AA}$  (87 keV); a beam spot of  $200 \times 200 \mu\text{m}^2$  at room temperature, and a two-dimensional (2D) detector PERKIN ELMER XRD 50 1621 was placed at 1.00 m from the samples. The raw 2D images were treated using Fit2D program (Hammersley, 1996) to calculate the individual XRD patterns by integration from  $0^\circ$  to  $360^\circ$  (azimuthal angles).

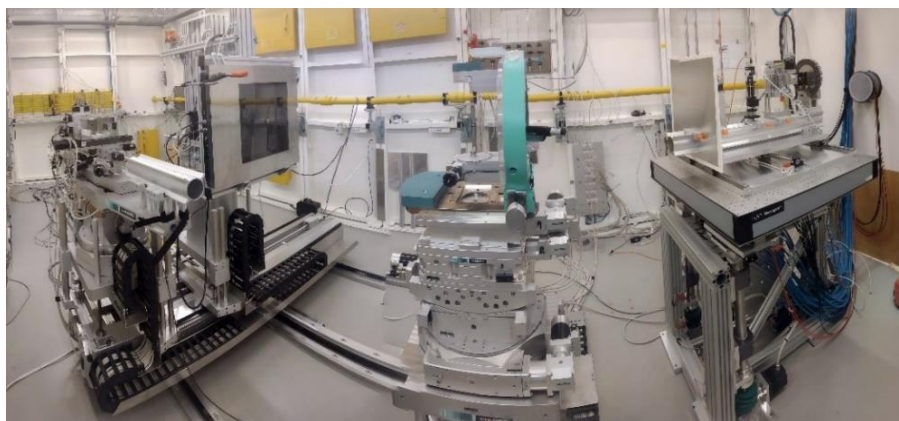


Figure 20- DESY PETRAIII: High Energy X-Ray Diffraction [47].

### 3.2.5.1. Differential Scanning Calorimetry (DSC)

Differential Scanning Calorimetry (DSC) is a thermal analysis technique used to study heat flow in or out of a sample.

DSC analysis is very important in order to study the martensitic transformation of the heat treated films. This fact is relevant for many reasons, being one of them to know at which temperatures a film is in the austenitic phase and if those temperatures are satisfactory for certain applications, namely for MEMS.

In a first run, to simulate the heat treatment, the sample was heated to 400 °C at a continuous heating rate of 10 °C/min followed by cooling to room temperature at a cooling rate of 10 °C/min. The first run was used to identify the possibility of the occurrence of some exothermic phenomenon. Immediately after the first run, the same sample was heated to 150 °C and subsequently cooled to -150 °C, again heated to 150 °C, and then cooled to room temperature. In the second run (up to 150 °C / -150 °C / 150 °C / Room Temperature) the phase transformation temperatures were determined by the tangent method. The DSC equipment used was DSC 204 F1 Phoenix from Netzsch in NOVA School of Science and Technology – NOVA FCT.

### 3.2.5.2. Nanoindentation

Nanoindentation is a type of depth sensing indentation technique that works with low displacements and forces to evaluate mechanical properties such as hardness and Young's modulus. This technique works by pressuring a calibrated diamond indenter against the sample, measuring its response and accordingly calculating the sample's mechanical properties, namely the hardness and the reduced Young's modulus.

Equation (3) allows to obtain the Young's modulus from the measured reduced Young's modulus. For that, it is necessary to know the Poisson coefficient of the material and diamond,  $\nu$  and  $\nu_i$ , respectively; as well as the Young's modulus of diamond ( $E_i$ ) [28].

$$\frac{1}{E_r} = \frac{(1 - \nu^2)}{E} + \frac{(1 - \nu_i^2)}{E_i} \Leftrightarrow E = \frac{(1 - \nu^2)}{\frac{1}{E_r} - \frac{(1 - \nu_i^2)}{E_i}} \quad (3)$$

The MicroMaterials nanoindentation equipment used (Figure 21) has a Berkovich indenter and can function in two modes: load control or indentation depth control. The nanoindentation experiments were performed in load control mode using a maximum load

of 5 mN. The maximum load was selected to make sure that the influence of the substrate is avoided, by guaranteeing that the maximum depth is below 10% of the films' total thickness [29,30]. A minimum of 30 indentations were performed in each sample. The results were treated according to Oliver & Pharr method [28], including thermal drift correction to compensate for the effects of temperature changes during the tests.

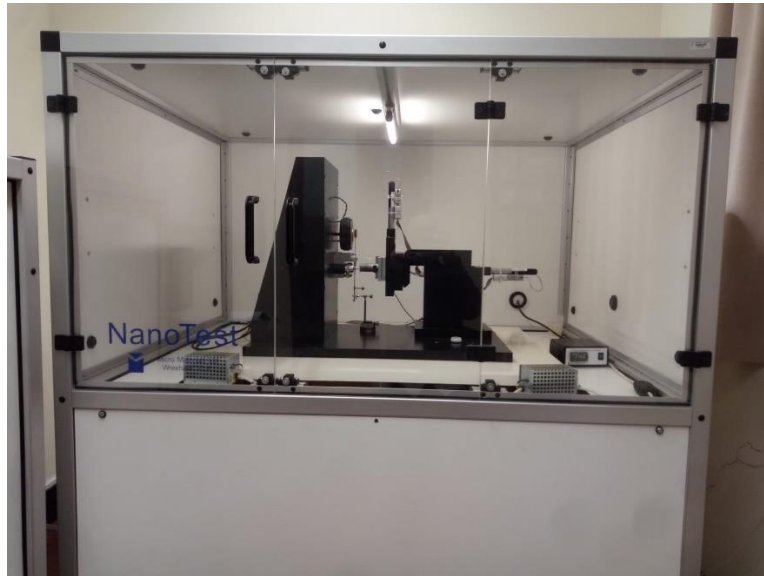


**Figure 21- DEM Nanoindentation equipment.**





## 4. RESULTS AND DISCUSSION

### 4.1. Chemical, morphological, structural and thermophysical characterization of the as-deposited films

#### 4.1.1. Energy Dispersive X-Ray Spectroscopy

After performing the EDS analysis, each film chemical composition was obtained as presented in Table 4.

Table 4- As-deposited films' chemical composition.

Film ID	Target(s)	Ni [at.%]	Ti [at.%]	V [at.%]
M0.3_1000	NiTi	60.7	39.3	—
M0.3_1700	NiTi	61.4	38.6	—
M0.5_1000	NiTi	60.3	39.7	—
M0.3_1000t	NiTi	59.4	40.6	—
ML_4	Ti/Ni	48.7	47.9	3.4

As can be observed, all the films are enriched in nickel. monolithic films have Ni atomic percentages close 60, while multilayer films have a near equiatomic NiTi chemical composition (50.4 at.% Ni, without considering vanadium). The use of an alloy target should result in films with chemical composition similar to the target [48]. However, due to the higher sputtering yield of Ni compared to Ti (more than double), the monolithic films have Ni contents much higher than the target from which they were prepared, in accordance with the available literature [19,20]. This Ni-rich chemical composition is required to reach the original objective of obtaining superelastic films [1,6]. Comparing with the reference film (M0.3\_1000), the increase of the power applied to the NiTi target led to a slight increase of the Ni content, while the increase of the deposition time results in a slightly lower Ni %. At the beginning of the sputtering process, more nickel atoms are ejected from the target, but as the target's surface become depleted in Ni, more titanium atoms are ejected, and in some cases a steady state where the films' chemical composition is close to the target's chemical

composition can be reached. In this study, the steady state was not reached, although the film deposited during 120 min has somewhat more Ti.

#### 4.1.2. Scanning Electron Microscopy

SEM analyses were made to characterize both surface and cross-section morphology of the as-deposited films.

In Figure 22 several micrographs are shown corresponding to the surface morphology of all the as-deposited films.

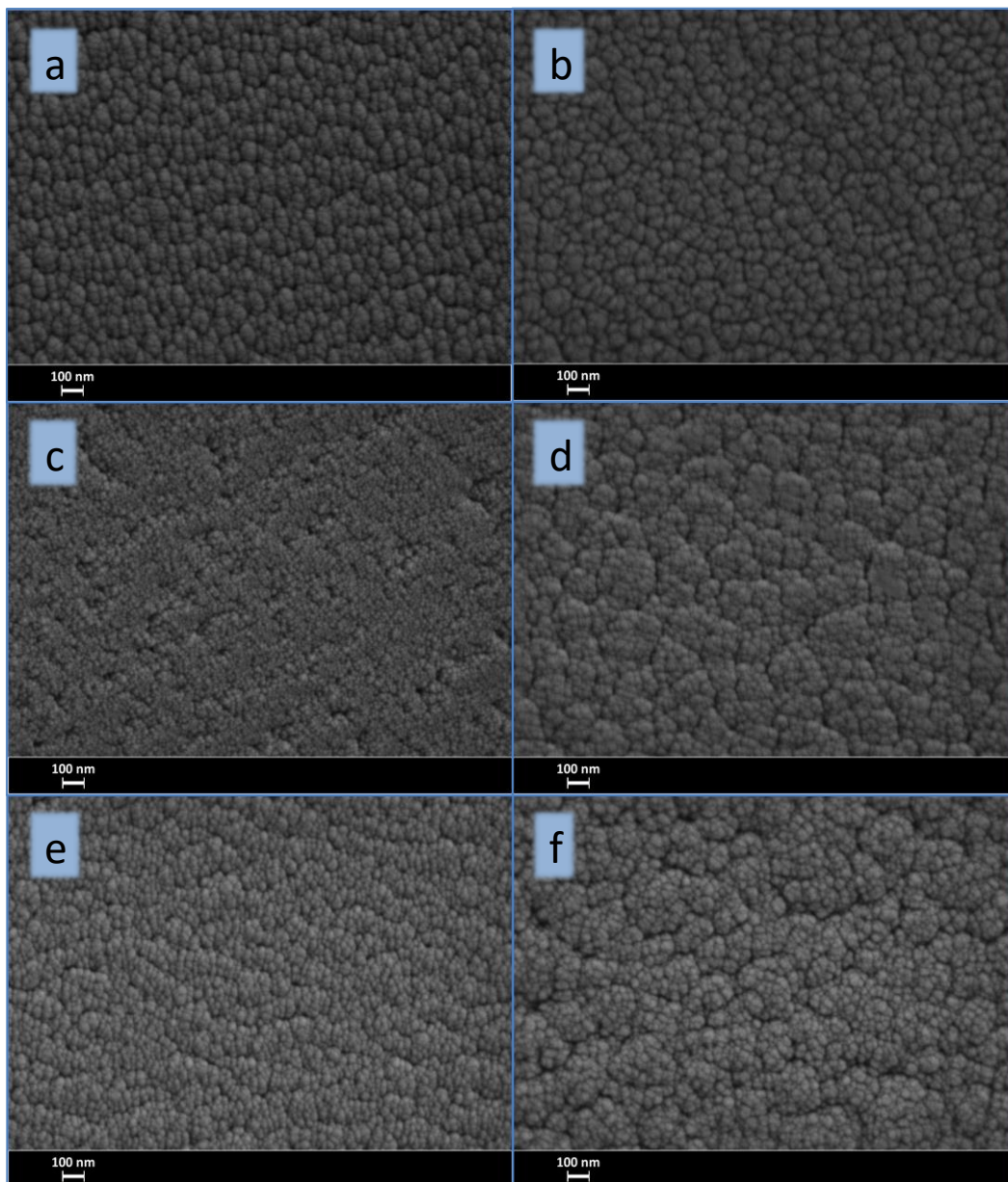


Figure 22- SEM surface images of as-deposited films: a) M0.3\_1000, b) M0.3\_1700, c) M0.5\_1000, d) M0.3\_1000t, e) ML\_4, f) ML\_60.

In all SEM images, except for the film deposited at a higher pressure, a cauliflower shape morphology can be observed, where the larger features should correspond to the top of the columns and, inside these features, some grains can be distinguished. This type of morphology is typical of metallic films deposited by magnetron sputtering, which usually results in columnar growth [49]. According to John A. Thornton [16], columnar cross-section morphologies are possible for specific deposition parameters, as it can be observed in Figure 7. In the SEM image corresponding to the M0.5\_1000 film (Figure 22c), the cauliflower morphology is not noticeable, having this film a smoother and dense surface morphology instead. SEM images of the monolithic films M0.3\_1000 and M0.3\_1700 show smaller surface features compared to the M0.3\_1000t and multilayer films. In particular, the film deposited during a longer time and the multilayer with a higher period exhibited larger features, corresponding to wider columns as can be confirmed in the cross-section images presented in Figure 23. According to the surface images of the multilayer films, the film with the higher period seems to have larger grain size, as expected due to the higher individual layer thicknesses.

Regarding the cross-section morphology, the highest pressure film (Figure 23c) has a dense columnar morphology and a higher thickness than the film deposited at a lower pressure keeping all the other parameters constant (M0.3\_1000). Higher pressure means more  $\text{Ar}^+$  ions bombarding the target(s) surface, and more collisions of the ejected atoms when travelling towards the substrates. In the present case, the first effect prevailed and an increase of the thickness was observed for the film deposited using a higher pressure. Looking at the rest of the monolithic films, an interesting characteristic can be observed, in particular for the film deposited applying a higher power to the NiTi target. In the SEM image of the M0.3\_1700 film (Figure 23b) vein-like features can be observed, which are characteristic of metallic glass thin films produced by sputtering [50,51]. The higher power should be responsible for the more notorious vein-like morphology in the M0.3\_1700 film. Nevertheless, by increasing the magnification, the observation of the vein-like morphology is also confirmed in other monolithic films (Figure 24). This morphology points to a more ductile behavior of the monolithic films when compared to the multilayer ones. The influence of deposition time can be seen when comparing films M0.3\_1000 and M0.3\_1000t at the same magnification (Figure 23a and 24b). Besides the obvious higher thickness,

M0.3\_1000t film has wider columns, as expected as time increases due to the shape of the columns.

When it comes to the multilayer films, a typical columnar cross-section morphology is observed (Figure 23e and 23f). In the multilayer film with the highest period (ML\_60) it is also possible to distinguish the alternating layers of nickel and titanium throughout the entire thickness and to confirm the estimated modulation period.

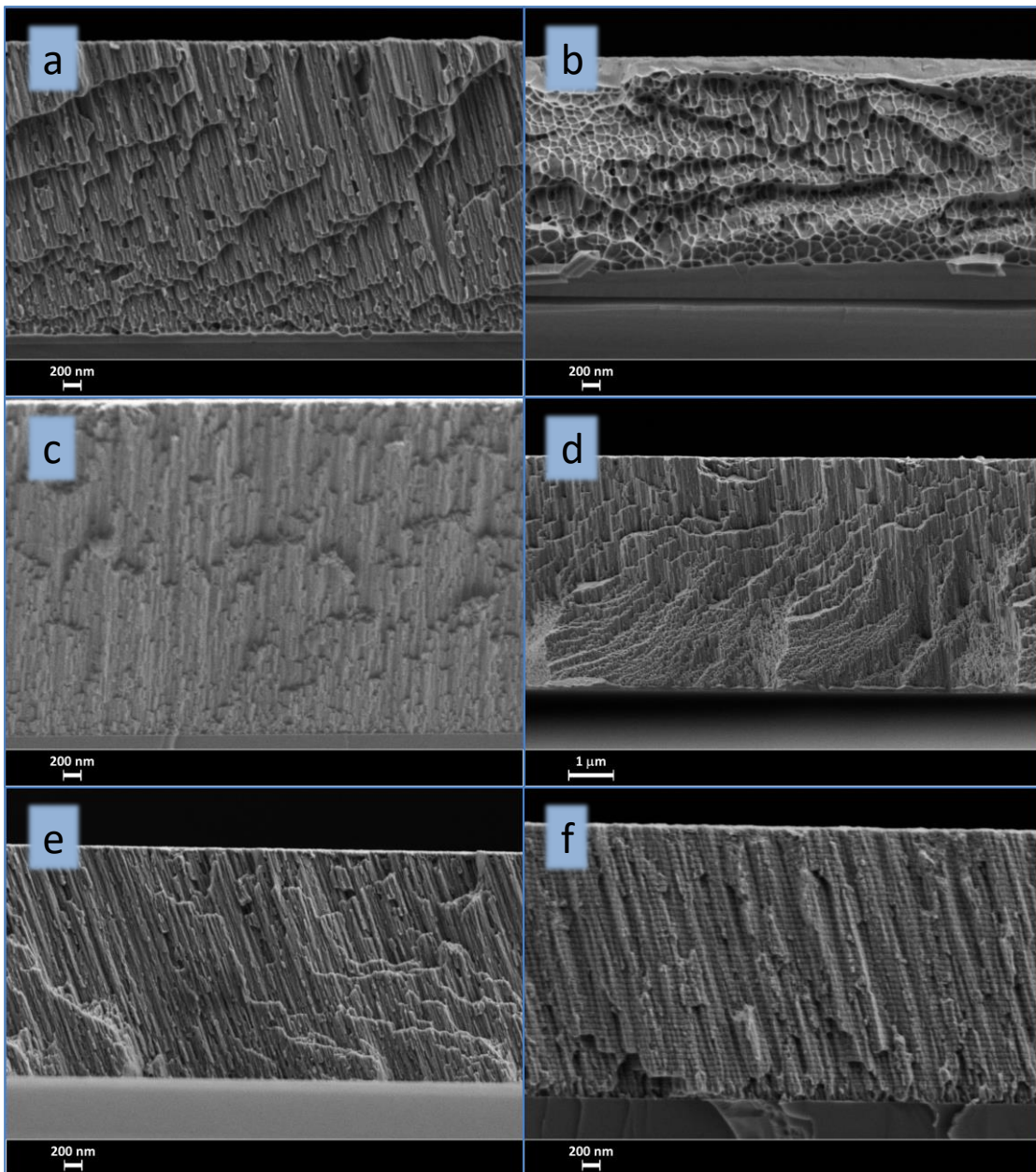


Figure 23- SEM cross-section images of as-deposited films: a) M0.3\_1000, b) M0.3\_1700, c) M0.5\_1000, d) M0.3\_1000t, e) ML\_4, f) ML\_60.

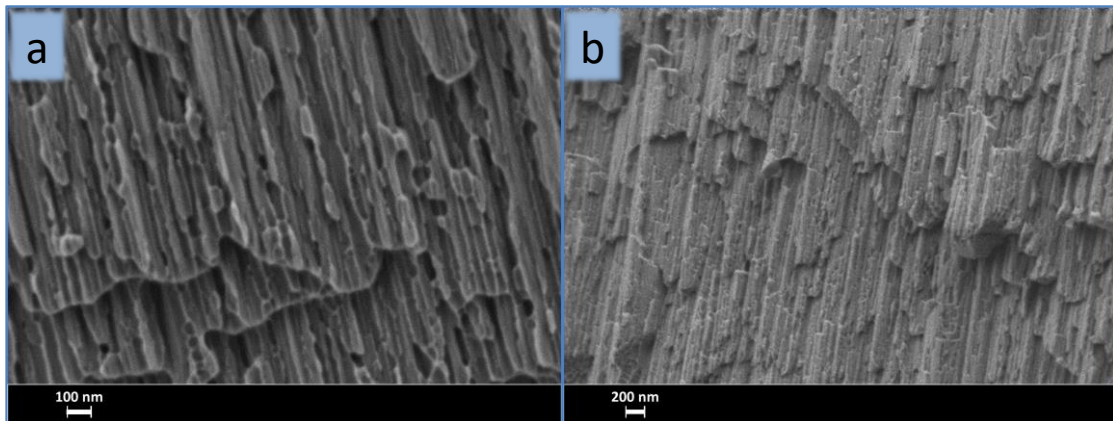


Figure 24- SEM cross-section image (higher magnification) of as-deposited films: a) M0.3\_1000 and b) M0.3\_1000t.

#### 4.1.3. X-ray diffraction

Analyzing the XRD diffractograms corresponding to the monolithic films (Figure 25a and 25b), it can be observed that both, conventional source and synchrotron radiation diffractograms indicate that the films exhibit a single broad peak. This observation suggests the absence of crystalline phases, leading to the conclusion that the as-deposited monolithic films in this study are amorphous. In the films deposited with the NiTi target, titanium and nickel atoms were simultaneously detached from that target and then deposited onto the substrate. Since the substrates were not heated, a rather low substrate temperature is expected, resulting in a low degree of crystallization of the mixture of nickel and titanium atoms, leading to amorphous films. The amorphous nature of as deposited films sputtered from NiTi targets without substrate heating has been reported in the literature [19,20].

Examining the diffractograms of the multilayer films (Figure 26a and 26b), a distinct situation is observed. Opposing to the monolithic films, multilayer films display defined XRD peaks. Two narrow and intense peaks are associated with the presence of crystalline phases. In this case the indexed planes are Ti (10.1) (lower angle XRD peak) and Ni (111) (higher angle XRD peak)

In films deposited with separated metallic targets, titanium and nickel atoms are detached from the targets and deposited to the substrate in an alternating pattern, which results in alternating nickel and titanium layers as shown in the SEM cross-section images (Figure 1 | Figure 23). It should be noted that using the copper substrate holders, the deposition temperatures attained are not sufficient to promote the reaction between Ni and Ti that occurs

above 350°C [4]. This translates in crystallized alternating layers of hcp titanium and fcc nickel, as evidenced by the multilayer diffractograms (Figure 26a and 26b).

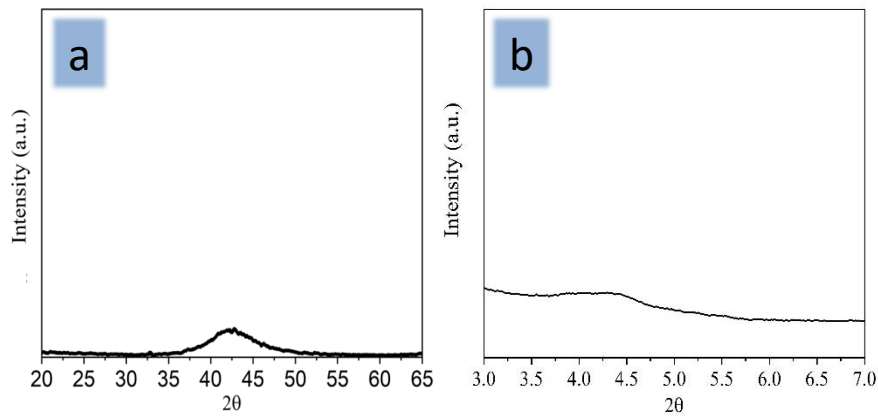


Figure 25- XRD diffractograms of as-deposited monolithic films: a) M0.3\_1000 (conventional XRD) and b) M0.3\_1700 (synchrotron energy XRD).

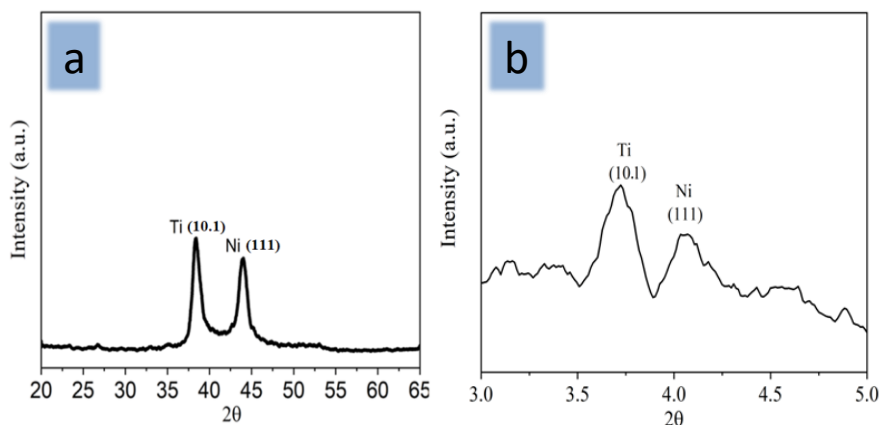


Figure 26- XRD diffractograms of as-deposited multilayer ML\_60 film: a) conventional XRD and b) synchrotron energy XRD.

#### 4.1.4. Differential Scanning Calorimetry

As mentioned in section 3.2 - Methods, after the deposition, the as-deposited films were subjected to a heat treatment, with the intent of forming crystalline phases, specifically austenite (B2-NiTi).

In an initial approach, a heat treatment was performed during the DSC analysis on the monolithic film M0.3\_1700, in order to study the possible occurrence of endothermic and exothermic phenomena hinting that some phase transition(s) can be identified.

The DSC heat treatment temperature chosen was 400°C because this is also the main heat treatment temperature selected for the subsequent morphological, structural and mechanical characterization.

Figure 27 presents the result of the DSC: a chart of heat flow versus temperature, where the temperature ranges from room temperature (about 25°C) to 400°C (673K). In this temperature range it is possible to verify some constant exothermal phenomenon. “The amorphous films crystallize when they are annealed at a temperature above 673K” (Otsuka, 1998) [52], so it is very plausible that said phenomenon is crystallization. After the initial stabilization, close inspection of the graph shows a heating evolution with a significant disruption of heat flow in temperatures from 80°C to 175°C. This behavior reveals the occurrence of some exothermal phenomenon before complete crystallization.

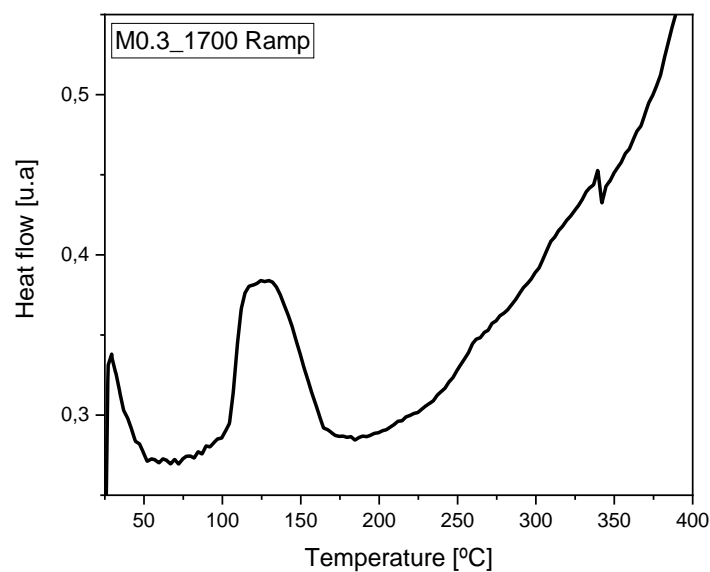


Figure 27- DSC ramp of film M0.3\_1700 during heat treatment.

## 4.2. Morphological, structural and thermophysical characterization of heat treated films

### 4.2.1. Scanning Electron Microscopy after heat treatment

After heat treatment, the surface and cross-section of the films was analyzed by SEM.

Looking at the surface heat treated SEM micrograph of Figure 28 and comparing with the surface as-deposited SEM image of Figure 22, it can be perceived that in monolithic film M0.3\_1000, the features observed are larger and the surface of the film seems more compact with the voids between the columns less defined. During heat treatment grain growth should also occur. The surface SEM image of the multilayer film with the highest period also reveal more compact morphology and less defined voids between columns. In the ML\_60 film the cauliflower morphology and the grains are barely distinguished. In addition, some light-colored spots can be observed in Figure 28b, that might correspond to some Ni-rich precipitates.

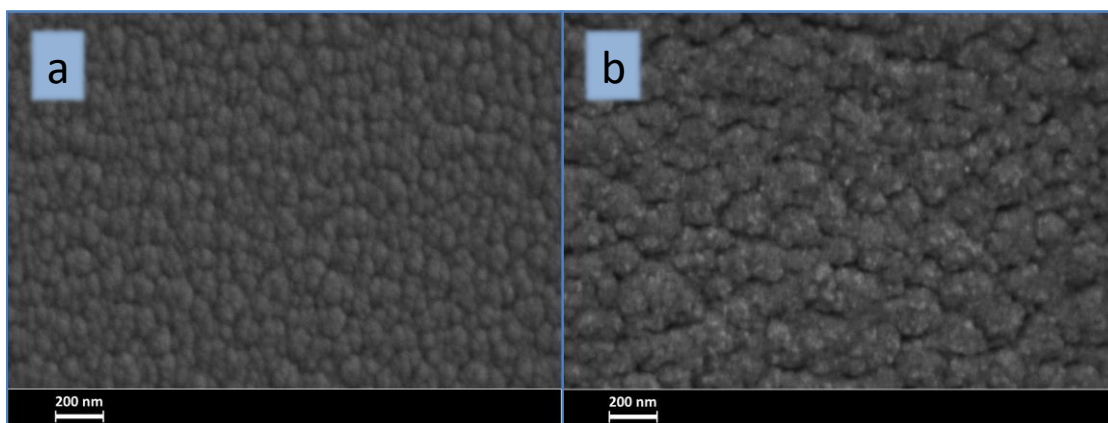


Figure 28- SEM surface images of heat treated films: a) M0.3\_1000 and b) ML\_60.

Cross-section SEM images of the heat treated films are shown in Figure 29. When analyzing the cross-section of the M0.3\_1700 monolithic film, there is a clear change from the as-deposited to the heat treated morphology. Although still with a slight vein-like appearance, heat treated M0.3\_1700 transitioned to a more compact morphology, confirmed by the thickness decrease from 2.7 to 2.3  $\mu\text{m}$ . A thin layer of oxide seems to have formed at the surface of the film.



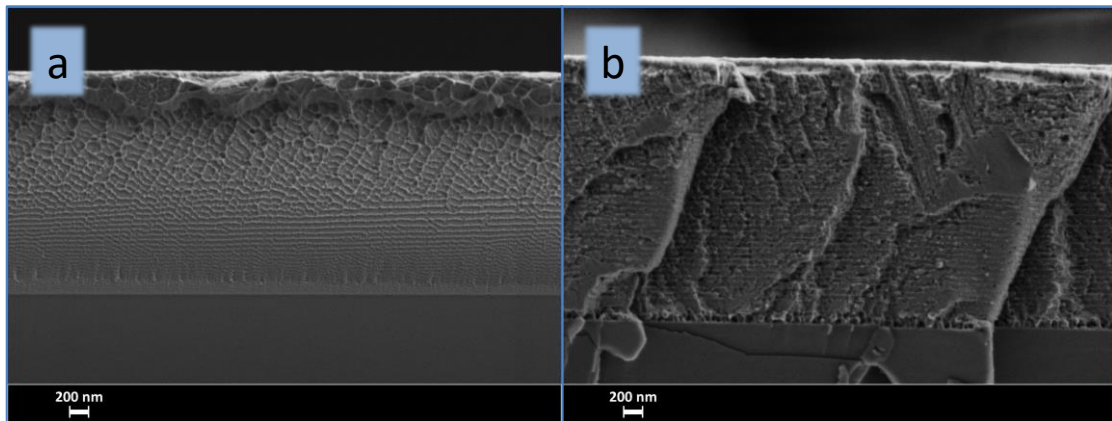


Figure 29- SEM cross-section image of heat treated films: a) M0.3\_1700 and b) ML\_60.

In the heat treated ML\_60 film cross-section SEM image, a more compact morphology can be clearly seen, with only traces of the initial columnar morphology. Again, the heat treatment promoted a decrease of thickness, in line with the observed densification. Although reaction between Ni and Ti occurred, the film still exhibits a layered structure, although less pronounced than the as-deposited alternating titanium and nickel layers (Figure 29b versus Figure 23f). However, there are regions with the same tone of color where nickel and titanium seem to have fully reacted.

#### 4.2.2. X-Ray Diffraction

After heat treatment, XRD analyses were conducted to ensure if the monolithic films had crystallized and if the multilayer films had reacted to form intermetallic phases, in particular the desired B2-NiTi phase. Since all the films are enriched in nickel, besides the austenitic phase, the indexation of Ni-rich crystalline phases is possible.

For the monolithic films (Figure 30) a change in the XRD diffractogram is clear. Films that were initially amorphous were found to crystallize revealing numerous XRD peaks. Among these, several were indexed as B2-NiTi, while a few can be identified as Ni-rich precipitates [52,53,54].

Initially, as-deposited multilayer films (Figure 26) correspond to crystalline hcp Ti and fcc Ni as exposed in section 4.1.3. With heat treatment, these crystals were proven to react forming B2-NiTi, and a high intensity B2 (110) peak can be observed (Figure 31). Although to less extent than in the monolithic films, minor XRD peaks that might correspond to Ni-rich precipitates can be observed in Figure 31. This finding is in accordance with the

EDS results (Table 4), which reveal that the average chemical composition of the multilayers films is only slightly enriched in Ni, while the monolithic films have Ni contents close to 60 at.%. Furthermore, B19' martensite phase might be indexed in the conventional diffractogram, which can also be present on synchrotron XRD merged with the B2 (110) austenite peak. In the literature, this phase was proven to appear as a result of induced stress [55].

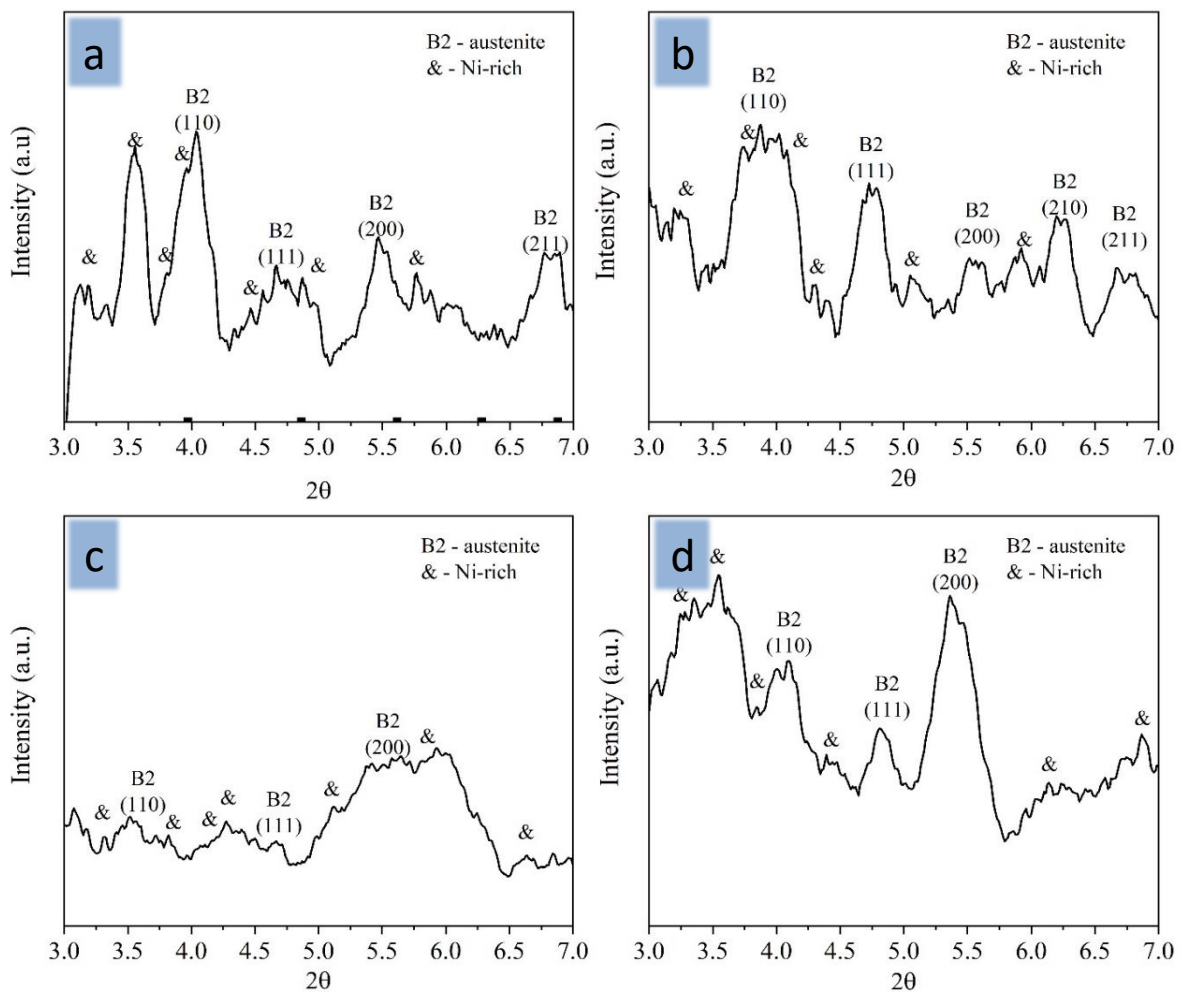


**Figure 30- Synchrotron XRD diffractograms of heat treated monolithic films: a) M0.3\_1000 b) M0.3\_1700 c) M0.5\_1000 d) M0.3\_1000t.**

The information of the XRD diffractograms is valuable because it proves that the chosen heat treatment temperature (400°C) is enough to form the B2 phase, the main driving factor for the existence of a superelastic NiTi film. The formed austenite present (110) and (111) crystallographic planes for all the films, having the monolithic films extra austenite crystallographic planes such as (200) and (211). Furthermore, along with austenite phase,

heat treatment temperature allowed the formation of Ni-rich precipitates (highlighted by & in Figure 30 and Figure 31), which can be interesting to improve the mechanical behavior of the films [56].

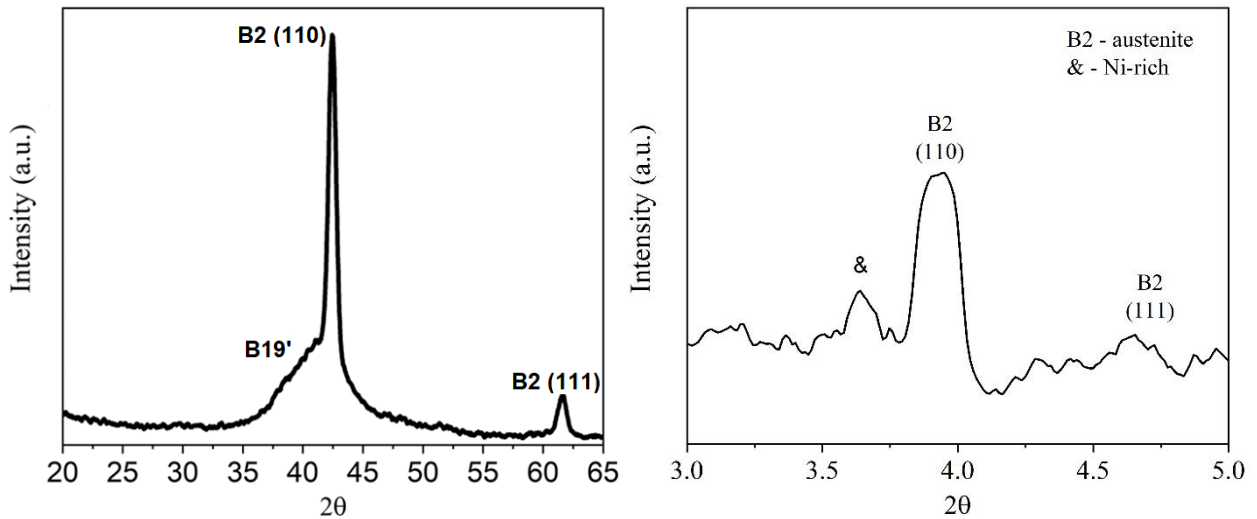


Figure 31- XRD diffractograms of heat treated multilayer ML\_60 film: conventional XRD on the left and synchrotron energy XRD on the right.

#### 4.2.3. Differential Scanning Calorimetry after heat treatment

DSC technique was applied on heat treated films to observe the phase transformations and estimate the respective temperatures.

By examining the DSC curves corresponding to the monolithic films (M0.3\_1000, M0.3\_1700 and M0.3\_1000t), and to the multilayer films (Figure 32) a common feature can be distinguished. In all the above-mentioned films there are only two clear heat flow tendency changes: one during cooling (at around  $-70^{\circ}\text{C}$ ) and one during heating (at around  $-90^{\circ}\text{C}$ , except for the film M0.3\_1700). This heat flow tendency suggests that there is one phase transition present per thermal process represented in the graph. It should be noted that it was extremely difficult to detach the films from the silicon substrates; therefore, the DSC signal corresponding to the films is weak, since the mass analyzed contained considerable amounts of Si. Another fact worth to be mentioned is that all the phase transitions occur at considerably negative temperatures.

As present at this point of the thesis, all the films are nickel-rich. Revisiting Figure 3 and its contextualization in the State of Art, rising of Ni at.% brings phase transformation temperatures down [6]. The slope is so high that nearly only titanium-rich and equiatomic materials have some of the transformation temperatures in the positive side.

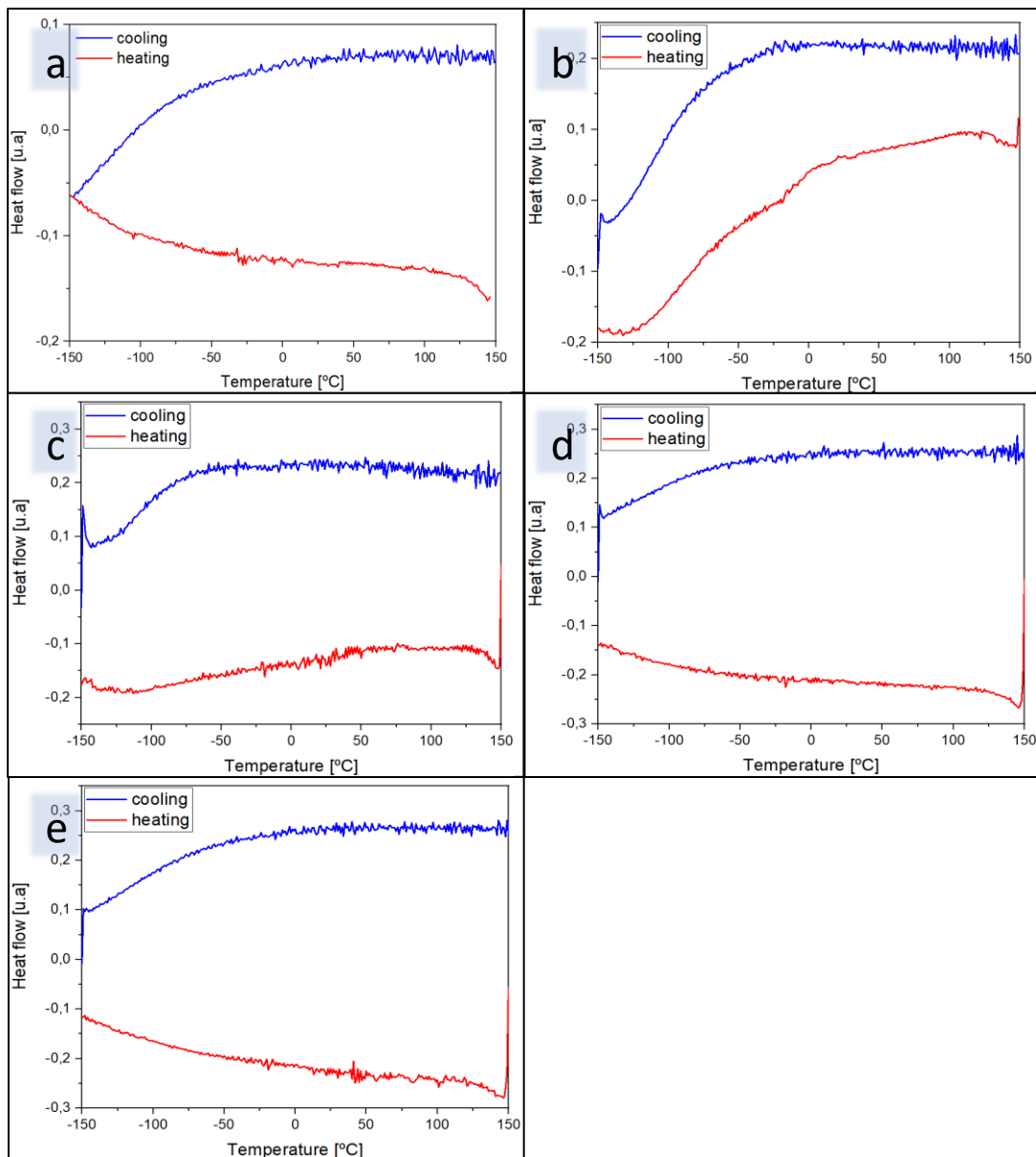


Figure 32- DSC curves of heat treated films: a) M0.3\_1000, b) M0.3\_1700, c) M0.3\_1000t, d) ML\_4, e) ML\_60.

Since the DSC equipment only has definition to study heat flows in a temperature range of  $-150^{\circ}\text{C}$  to  $150^{\circ}\text{C}$ , with the previous sentence in mind, it is certain that every film under study has low phase transition temperatures. This means that in most application temperatures, including room temperature, the temperatures are higher than  $A_f$ , meaning that the film is in the in austenitic field. This accomplishment is one of the main goals of this thesis, whose objective is to have superelastic NiTi films for MEMS applications.

The DSC curve of the M0.5\_1000 film (Figure 33) has a quite different appearance, showing one phase transition temperature for the cooling and four for the heating. When it

comes to the cooling process, it appears to follow the same negative temperature deviation of the remaining films. For the heating process, however, two complete phase transformations are present, one corresponding to the intermediate phase (R-phase) transformation with  $R_s \approx -110^\circ\text{C}$  and  $R_f \approx -80^\circ\text{C}$ , and the other to the austenite phase transformation with  $A_s \approx 30^\circ\text{C}$  and  $A_f \approx 100^\circ\text{C}$ . The R-phase can be interesting in a variety of specific applications, due some distinct characteristics, such as phase transformation temperature and mechanical behavior.

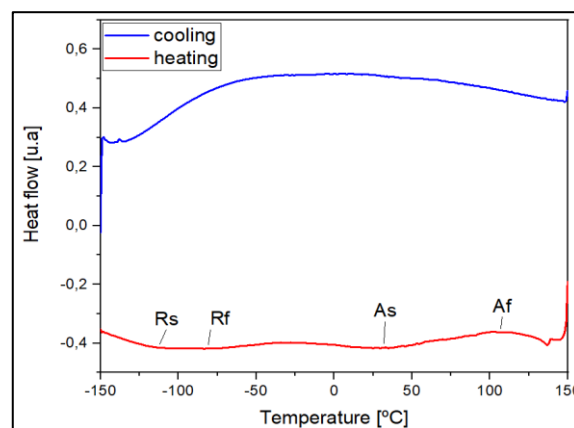


Figure 33- DSC curve of M0.5\_1000 heat treated film.

### 4.3. Mechanical Properties

To study the mechanical behavior, the nanoindentation technique was used in order to obtain films' hardness and Young's modulus.

Table 5 shows the average mechanical properties of the as-deposited films with the respective standard deviations, while Table 6 shows the mechanical properties of heat treated films. As can be seen in Table 5, the maximum indentation depths are always below 10% of the films' thickness, assuring that there is no influence of substrate on the hardness values.

For the monolithic films M0.3\_1000 and M0.3\_1700, a hardness of around 9 GPa and a Young's modulus of about 150 GPa was registered for both, meaning that the power applied to the NiTi target does not significantly influence the films' mechanical behavior. In fact, these films have similar nickel content and similar surface morphology.

**Table 5- Mechanical behavior of as-deposited films**

Film	Thickness [ $\mu\text{m}$ ]	Max Depth, $h_p$ [nm]	Plastic Depth [nm]	Hardness, H [GPa]	Er, [GPa]	Young Mod, E [GPa]
M0.3_1000	3.2	139.3 $\pm$ 4.5	109.3 $\pm$ 5.2	9.1 $\pm$ 0.6	145 $\pm$ 6	153 $\pm$ 6
M0.3_1700	2.7	138.2 $\pm$ 8.2	107.5 $\pm$ 8	9.3 $\pm$ 0.9	144 $\pm$ 10	152 $\pm$ 10
ML_4	2.5	154.3 $\pm$ 4.7	124.3 $\pm$ 5.1	7.6 $\pm$ 0.4	133 $\pm$ 5	139 $\pm$ 5
ML_60	3.0	153.8 $\pm$ 6.8	124.8 $\pm$ 7.0	7.6 $\pm$ 0.6	137 $\pm$ 7	143 $\pm$ 7

**Table 6- Mechanical behavior of heat treated films.**

Film	Max Depth, $h_p$ [nm]	Plastic Depth [nm]	Hardness, H [GPa]	Er, [GPa]	Young Mod, E [GPa]
M0.3_1000 400C	129.2 $\pm$ 4.7	99.2 $\pm$ 5.0	10.3 $\pm$ 0.7	155 $\pm$ 5	165 $\pm$ 5
M0.3_1700 400C	128.7 $\pm$ 3.9	98.8 $\pm$ 4.3	10.4 $\pm$ 0.6	156 $\pm$ 6	167 $\pm$ 6
ML_4 400C	136.1 $\pm$ 5.8	105.8 $\pm$ 6,1	9.5 $\pm$ 0.7	147 $\pm$ 7	155 $\pm$ 7
ML_60 400C	140.5 $\pm$ 3.7	104.5 $\pm$ 4.3	9.6 $\pm$ 0.5	124 $\pm$ 4	128 $\pm$ 4
ML_60 500C	147.7 $\pm$ 3.5	111.7 $\pm$ 4.1	8.8 $\pm$ 0.4	119 $\pm$ 2	122 $\pm$ 2

For both multilayer films a hardness of 7.6 GPa and a Young's modulus of about 140 GPa was registered. When comparing multilayer films with different modulation periods, the expected trend is that represented in Figure 9 in the State of Art: the hardness decreases as the period increases, except for very short periods where the reverse occurs [33]. The shortest period studied in this work (4 nm) should fall in the region where the hardness decreases as the period decreases, while the 60 nm period is already in the region where the hardness decreases as the period increases. At the end, the multilayer films have similar hardness values, although in different regions of the hardness curve as function of the period.

An interesting observation is that the hardness of the multilayer films is significantly higher than the result of the rule of mixtures considering the hardness of Ti and Ni pure films. This fact is reported multiple times in the literature of multilayer films (e.g. [57]) and has been proven to be a result of the presence of multiple interfaces and of the low individual layer thicknesses, which limits grain growth resulting in smaller grains. According to the Hall-Petch law, grain size is inversely proportional to the hardness, meaning that low grain size will increase film's hardness. Regarding the Young's modulus of the multilayer films the values should obey to the rule of mixtures since it is an intrinsic mechanical property that

in principle should only depend on the chemical bonding. The Young's modulus obtained for an equiatomic Ni/Ti multilayer using a rule of mixtures is 160 GPa [58,59], a value somewhat higher than the values in Table 6.

Heat treating the films promoted changes in their mechanical properties. For the hardness, a significant increase is observed, as illustrated in Figure 34 and Figure 35.

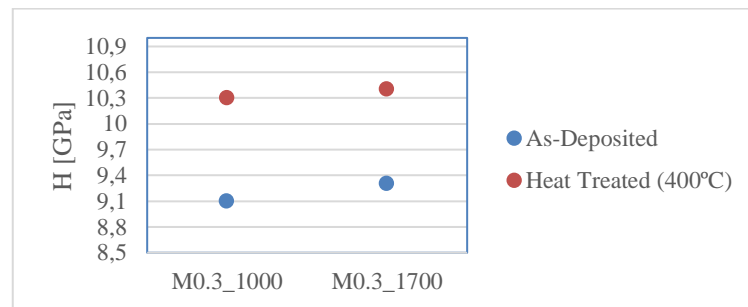


**Figure 34-Hardness of as-deposited and heat treated (400°C) monolithic films.**

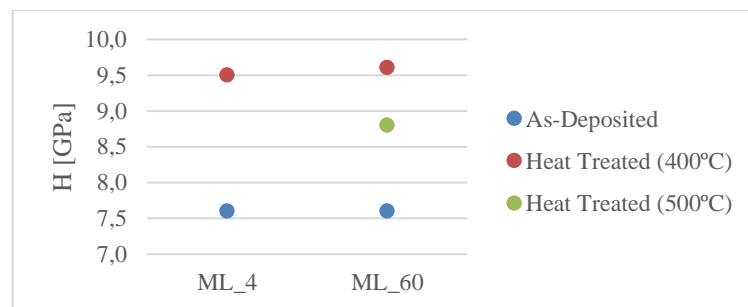


**Figure 35- Hardness of as-deposited and heat treated (400°C and 500°C) multilayer films.**

When analyzing films heat treated at 400°C, it is evident that hardness increased in every film: monolithic films had an increase of about 13% and multilayer films' hardness increased about 26%. This hardness increase is because heat treatment promotes the formation of hard intermetallic phases, but also induces compaction, as confirmed by SEM, which by itself increases hardness.

The heat treatment of the multilayer film ML\_60 at a higher temperature (500°C), gave rise to a lower increase in the hardness of the as-deposited film (~ 16%) The explanation behind this is the higher heat treatment temperature which promotes a more pronounced grain growth, when compared to the lower heat treatment temperature. According to the Hall-Petch's law, this fact lowers the hardness.

Regarding the Young's modulus monolithic and multilayer films have values higher than those found in the literature for equiatomic NiTi and Ni-rich materials (about 75GPa [60]). These films proven to have formed B2-NiTi as the major phase, which should have brought Young's modulus closer to the value indicated. The higher Young's modulus observed can be explained by the influence of the silicon substrate. Even though the maximum depths are lower than 10% of the thickness, when it comes to the Young's modulus, substrate's influence is still possible. Tests conducted using the same nanoindentation equipment also with a maximum load of 5 mN, reveal a reduced Young's modulus for monocrystalline silicon around 175 GPa. Therefore, if there is influence of the substrate it should result in higher Young's modulus that expected for NiTi films. In fact, when comparing the Young's modulus for the films ML\_4 and ML\_60 heat treated at 400°C, a higher value is observed for the thinner ML\_4 film, corroborating the hypothesis of substrate influence.

As an example, the indentation curves - load (P) versus indentation depth (h) - corresponding to the as-deposited and heat treated (400 and 500°C) ML\_60 film are shown in Figure 36.

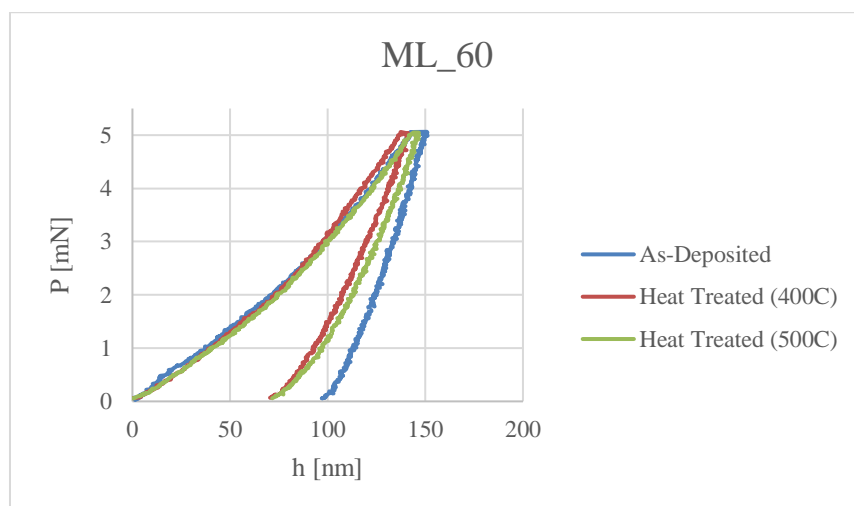
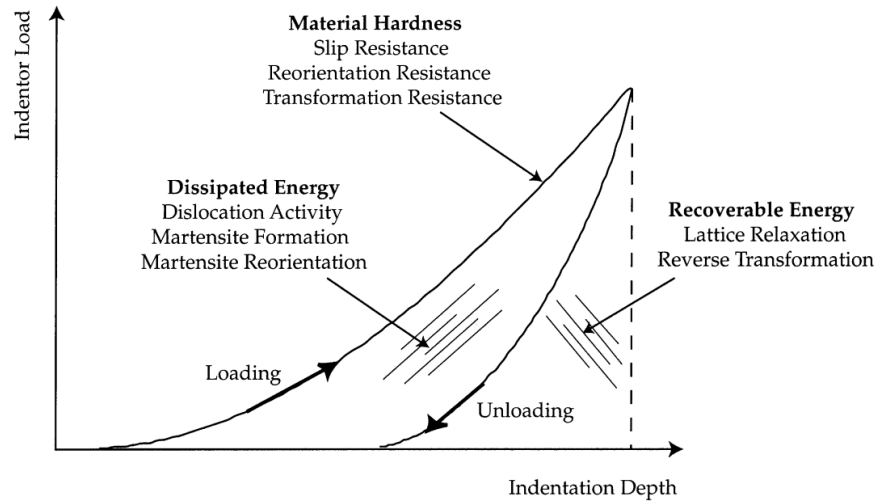


Figure 36- Indentation curves of the as-deposited and heat treated (400 and 500°C) ML\_60 film.

According to Gall et al [61], the unloading part of the indentation curve allows the recoverable energy to be analyzed (Figure 37). According to Figure 36, the ML\_60 film heat treated at 500°C reveals a higher elastic recovery than after the 400°C heat treatment (green



and red curves, respectively), indicating a higher quantity of B2-NiTi or a more homogeneous austenitic matrix, which might be favorable for MEMS applications.



**Figure 37- Scheme relating nanoindentation microstructural mechanisms with material hardness, energy dissipation and energy recovery for NiTi shape memory alloys [61].**



## 5. CONCLUSIONS

NiTi monolithic and Ni/Ti multilayer films were produced by magnetron sputtering, using different deposition parameters. Both, monolithic and multilayer films had to be heat treated to obtain the NiTi shape memory alloy.

From close analysis of all the results of this thesis, the following conclusions can be taken:

### 1. As-deposited Monolithic Films:

i) Contrary to the expected based on sputtering theory, monolithic films' chemical composition reveals higher nickel contents than the equiatomic NiTi target. In this study, a steady state that would result in films with the same chemical composition of the target from which they were sputtered was not reached.

ii) The increase of the power applied to the NiTi target results in films with a slightly higher Ni content.

iii) The films present a cauliflower-like surface morphology, except the film deposited at a higher pressure. The cross-section morphology of most films is columnar with traces of vein-like features. These vein-like features are dominant in the M0.3\_1700 film.

iv) After deposition all the films are amorphous, as usual in NiTi sputtered films without substrate heating.

v) The as-deposited monolithic films have higher hardness than the multilayer ones.

### 2. Multilayer Films:

i) Multilayer films' chemical composition can be successfully controlled by adjusting the power applied to each target. Films slightly enriched in Ni were produced.

ii) The modulation period of the multilayer films was adjusted by varying the substrates rotation speed. Periods of 4 and 60 nm were studied.

iii) The multilayer films also have cauliflower-like surface morphology, with larger features in the film with  $\Lambda = 60$  nm. The cross-section morphology is columnar and the films seem less ductile than the monolithic ones.

iv) The as-deposited multilayer films are crystalline. Fcc Ni and hcp Ti phases were identified.

v) The hardness and Young's modulus of the two multilayer films are similar. The hardness is significantly higher than the result of the rule of mixtures considering the hardness of Ti and Ni pure films.

### **3. Heat treated monolithic and multilayer films:**

i) Heat treatment promoted grain growth, thickness reduction and more compact films.

ii) In the highest period multilayer, although Ni and Ti reacted, it is still possible to observe a layered structure.

iii) The 400°C temperature was enough to promote the crystallization of the monolithic films with the formation of austenitic B2-NiTi as major phase, together with Ni-rich precipitates.

iv) During heat treatment Ni and Ti reacted forming B2-NiTi. In accordance with their chemical composition, the presence of other phases in heat treated multilayer films is less pronounced.

v) DSC analysis performed while heat treating an as-deposited monolithic film confirms the occurrence of crystallization (exothermic peak).

vi) The films under study reveal negative thermophysical transformation temperatures, meaning that a stable austenitic phase is present at room temperature.

vii) The heat treatment is responsible for a hardness increase. However, due to grain growth the film heat treated at 500°C had lower a hardness than the corresponding film treated at 400°C.

viii) Heat treatment also increases the Young's modulus of most of the films. An increase in heat treatment temperature of the highest period multilayer showed a slight increase in the elastic recovery.

Considering the conclusions above and the versatility of the sputtering technique, the NiTi films produced, especially the monolithic ones, show potential for MEMS applications. Nevertheless, there is still research work to be done.

## **Future Work**

In the course of this research many breakthroughs and discoveries were accomplished. However, as part of every research, new questions have emerged that will require further investigation.

### **1. Monolithic films:**

i) Study different interelectrode (target-substrates) distances, to obtain Ni-rich films, but limited to ~ 55 at.% of nickel.

ii) Study the influence of different deposition parameters on obtaining vein-like morphologies typical of metallic glasses, and their effect on the films' thermophysical and mechanical properties.

### **2. Multilayer films:**

i) Production of films with different periods, to study the influence on the thermophysical and mechanical properties.

### **3. Monolithic and multilayer films:**

i) Sputter deposit films with an interlayer between substrate and film, to facilitate the detachment of the films from the substrate and allow the thermophysical properties of free-standing films to be evaluated.

ii) Study the influence of higher heat treatment temperatures, namely on the films' elastic recovery.

iii) Study the films' superelasticity, having in mind their use in MEMS applications.



---

## REFERENCES

1. Otsuka K, Ren X. Physical metallurgy of Ti-Ni-based shape memory alloys. *Progress in Materials Science* 2005; 50: 511–678.
2. Tillmann W, Momeni S. Deposition of superelastic composite NiTi based films. *Vacuum* 2014; 104: 41–46.
3. Shih CL, Lai BK, Kahn H, Phillips SM, Heuer AH. A robust co-sputtering fabrication procedure for TiNi shape memory alloys for MEMS. *Journal of Microelectromechanical Systems* 2001; 10: 69–79.
4. Cavaleiro AJ, Santos RJ, Ramos AS, Vieira MTF. In-situ thermal evolution of Ni/Ti multilayer thin films. *Intermetallics* 2014; 51: 11–17.
5. Tarquino EAA. Structural fatigue of superelastic NiTi wires. 2018. PhD Thesis. Université de Bretagne Occidentale.
6. Frenzel J, George EP, Dlouhy A, Somsen C, Wagner MFX, Eggeler G. Influence of Ni on martensitic phase transformations in NiTi shape memory alloys. *Acta Materialia* 2010; 58: 3444–3458.
7. Marupalli BCG, Behera A, Aich S. A Critical Review on Nickel–Titanium Thin-Film Shape Memory Alloy Fabricated by Magnetron Sputtering and Influence of Process Parameters. *Transactions of the Indian Institute of Metals* 2021; 74: 2521–2540.
8. Andy Elliott - Nitinol. 2013 <https://www.youtube.com/watch?v=FBaIdvgbBAM> (8 September 2023, date last accessed).
9. Otsuka K, Kakeshita T. Science and Technology of Shape-Memory Alloys: New Developments. *MRS Bulletin* 2002; 27: 91–100.
10. Khanlari K, Ramezani M, Kelly P. 60NiTi: A Review of Recent Research Findings, Potential for Structural and Mechanical Applications, and Areas of Continued Investigations. *Transactions of the Indian Institute of Metals* 2018; 71: 781–799.
11. Xu GX, Zheng LJ, Zhang FX, Zhang H. Influence of solution heat treatment on the microstructural evolution and mechanical behavior of 60NiTi. *Journal of Alloys and Compounds* 2019; 775: 698–706.
12. Zhang F, Zheng L, Wang F, Zhang H. Effects of Nb additions on the precipitate morphology and hardening behavior of Ni-rich Ni55Ti45 alloys. *Journal of Alloys and Compounds* 2018; 735: 2453–2461.
13. Shu X, Hu L, Li G, Lu S, Wang K, Peng P. High-temperature oxidation resistance of the Ni60Ti alloy: An experimental and first-principles study. *Journal of Alloys and Compounds* 2017; 706: 297–304.
14. Khanlari K, Shi Q, Li K *et al.* Fabrication of Ni-Rich 58NiTi and 60NiTi from Elementally Blended Ni and Ti Powders by a Laser Powder Bed Fusion Technique: Their Printing, Homogenization and Densification. *International Journal of Molecular Sciences* 2022; 23: 9495.
15. Sanjabi S, Sadrnezhaad SK, Yates KA, Barber ZH. Growth and characterization of  $Ti_xNi_{1-x}$  shape memory thin films using simultaneous sputter deposition from separate elemental targets. *Thin Solid Films* 2005; 491: 190–196.
16. Thornton JA. The microstructure of sputter-deposited coatings. *Journal of Vacuum Science & Technology A: Vacuum, Surfaces, and Films* 1986; 4: 3059–3065.

17. Barron SC, Knepper R, Walker N, Weihs TP. Characterization of self-propagating formation reactions in Ni/Zr multilayered foils using reaction heats, velocities, and temperature-time profiles. *Journal of Applied Physics* 2011; 109: 013519.
18. Fu Y, Huang W, Du H, Huang X, Tan J, Gao X. Characterization of TiNi shape-memory alloy thin films for MEMS applications. *Surface Coatings and Technology* 2001; 145: 107–112.
19. Tillmann W, Momeni S. In-situ annealing of NiTi thin films at different temperatures. *Sensors and Actuators, A: Physical* 2015; 221: 9–14.
20. Sharma SK, Mohan S. Influence of annealing on structural, morphological, compositional and surface properties of magnetron sputtered nickel-titanium thin films. *Applied Surface Science* 2013; 282: 492–498.
21. Miyazaki S, Ishida A. Martensitic transformation and shape memory behavior in sputter-deposited TiNi-base thin films. *Materials Science and Engineering* 1999; 273-275: 106–133.
22. Bai X, Cai Q, Xie W, Zeng Y, Chu C, Zhang X. In-situ crystalline TiNi thin films deposited by HiPIMS at a low substrate temperature. *Surface and Coatings Technology* 2023; 455: 129196.
23. Cho H, Kim HY, Miyazaki S. Alloying process of sputter-deposited Ti/Ni multilayer thin films. *Materials Science and Engineering A* 2006; 438–440: 699–702.
24. Lehnert T, Grimmer H, Böni P, Horisberger M, Gotthardt R. Characterization of shape-memory alloy thin films made up from sputter-deposited Ni/Ti multilayers. *Acta Materialia* 2000; 48: 4065–4071.
25. Cavaleiro AJ, Ramos AS, Martins RMS *et al.* Phase transformations in Ni/Ti multilayers investigated by synchrotron radiation-based x-ray diffraction. *Journal of Alloys and Compounds* 2015; 646: 1165–1171.
26. Kumar A, Singh D, Kaur D. Grain size effect on structural, electrical and mechanical properties of NiTi thin films deposited by magnetron co-sputtering. *Surface and Coatings Technology* 2009; 203: 1596–1603.
27. Ramos AS, Cavaleiro AJ, Vieira MT, Morgiel J, Safran G. Thermal stability of nanoscale metallic multilayers. *Thin Solid Films* 2014; 571: 268–274.
28. Oliver WC, Pharr GM. Measurement of hardness and elastic modulus by instrumented indentation: Advances in understanding and refinements to methodology. *Journal Materials Research* 2004; 19: 3-20.
29. Logothetidis S, Charitidis C. Elastic properties of hydrogen-free amorphous carbon thin films and their relation with carbon-carbon bonding. *Thin Solid Films* 1999; 353: 208–213.
30. Fasaki I, Koutoulaki A, Kompitsas M, Charitidis C. Structural, electrical and mechanical properties of NiO thin films grown by pulsed laser deposition. *Applied Surface Science* 2010; 257: 429–433.
31. Behera A, Rajak DK, Kolahchi R, Scutaru ML, Pruncu CI. Current global scenario of Sputter deposited NiTi smart systems. *Journal of Materials Research and Technology* 2020; 9: 14582–14598.
32. Tillmann W, Momeni S. Comparison of NiTi thin films sputtered from separate elemental targets and Ti-rich alloy targets. *Journal of Materials Processing Technology* 2015; 220: 184–190.



33. Wen SP, Zeng F, Gao Y, Pan F. Microstructure and nanoindentation investigation of magnetron sputtering Ag/Co multilayers. *Surface and Coatings Technology* 2006; 201: 1262–1266.
34. Martins JNR, Silva EJNL, Marques D *et al.* Design, Metallurgical Features, and Mechanical Behaviour of NiTi Endodontic Instruments from Five Different Heat-Treated Rotary Systems. *Materials* 2022; 15: 1009.
35. Justin Evans TW, Jones ML, Newcombe RG. Clinical comparison and performance perspective of three aligning arch wires. *American Journal of Orthodontics and Dentofacial Orthopedics* 1998; 114: 32–39.
36. Yuan B, Zhu M, Chung CY. Biomedical porous shape memory alloys for hard-tissue replacement materials. *Materials* 2018; 11: 1716.
37. Miller DJ, Fahnestock LA, Eatherton MR. Development and experimental validation of a nickel-titanium shape memory alloy self-centering buckling-restrained brace. *Engineering Structures* 2012; 40: 288–298.
38. Ozbulut OE, Hurlbauss S. Optimal design of superelastic-friction base isolators for seismic protection of highway bridges against near-field earthquakes. *Earthquake Engineering and Structural Dynamics* 2011; 40: 273–291.
39. Wu XD, Fan YZ, Wu JS. A study on the variations of the electrical resistance for NiTi shape memory alloy wires during the thermo-mechanical loading. *Materials and Design* 2000; 21: 511515.
40. Gurley A, Lambert TR, Beale D, Broughton R. Dual measurement self-sensing technique of NiTi actuators for use in robust control. *Smart Materials and Structures* 2017; 26: 105050.
41. Waddell AM, Punch J, Stafford J, Jeffers N. On the hydrodynamic characterization of a passive shape memory alloy valve. *Applied Thermal Engineering* 2015; 75: 731–737.
42. Xu D, Wang L, Ding G, Zhou Y, Yu A, Cai B. Characteristics and fabrication of NiTi/Si diaphragm micropump. *Sensors and Actuators A* 2001; 93: 87–92.
43. Daly M, Pequegnat A, Zhou YN, Khan MI. Fabrication of a novel laser-processed NiTi shape memory microgripper with enhanced thermomechanical functionality. *Journal of Intelligent Material Systems and Structures* 2013; 24: 984–990.
44. Barth J, Krevet B, Kohl M. A bistable shape memory microswitch with high energy density. *Smart Materials and Structures* 2010; 19: 094004.
45. Yang X, Chang L, Pérez-Arancibia NO. An 88-milligram insect-scale autonomous crawling robot driven by a catalytic artificial muscle. *Sci Robot* 2020; 5: 15.
46. B.D. Cullity, S.R. Stock. *Elements of X-Ray Diffraction*. Third Edition 2014.
47. Helmholtz Association. High Energy X-Ray Diffraction for Physics and Chemistry. [https://photon-science.desy.de/facilities/petra\\_iii/beamlines/p21\\_swedish\\_materials\\_science/p211\\_high\\_energy\\_x\\_ray\\_diffraction\\_for\\_physics\\_and\\_chemistry/index\\_eng.html](https://photon-science.desy.de/facilities/petra_iii/beamlines/p21_swedish_materials_science/p211_high_energy_x_ray_diffraction_for_physics_and_chemistry/index_eng.html) (8 September 2023, date last accessed).
48. Cavaleiro A, Vieira M. *Sebenta Engenharia de Superfícies e Degradação e Proteção de Superfícies*. 1995.
49. Gachon JC, Rogachev AS, Grigoryan HE *et al.* On the mechanism of heterogeneous reaction and phase formation in Ti/Al multilayer nanofilms. *Acta Materialia* 2005; 53: 1225–1231.

50. Apreutesei M, Steyer P, Billard A, Joly-Pottuz L, Esnouf C. Zr-Cu thin film metallic glasses: An assessment of the thermal stability and phases' transformation mechanisms. *Journal of Alloys and Compounds* 2015; 619: 284–292.
51. Chang JC, Lee JW, Lou BS, Li CL, Chu JP. Effects of tungsten contents on the microstructure, mechanical and anticorrosion properties of Zr-W-Ti thin film metallic glasses. *Thin Solid Films* 2015; 584: 253–256.
52. Otsuka K, Wayman CM. *Shape memory materials*. 1st Edition Cambridge University Press, 1998.
53. Somsen C, Zähres H, Kästner J, Wassermann EF, Kakeshita T, Saburi T. Influence of thermal annealing on the martensitic transitions in Ni-Ti shape memory alloys. *Materials Science and Engineering* 1999; 273-275: 310–314.
54. Hou H, Hamilton RF, Horn MW. Crystallization of nanoscale NiTi alloy thin films using rapid thermal annealing. *Journal of Vacuum Science & Technology B* 2016; 34: 06KK01.
55. Amini A, Yan W, Sun Q. Depth dependency of indentation hardness during solid-state phase transition of shape memory alloys. *Applied Physics Letters* 2011; 99.
56. Yu H, Qiu Y, Young ML. Influence of Ni<sub>4</sub>Ti<sub>3</sub> precipitate on pseudoelasticity of austenitic NiTi shape memory alloys deformed at high strain rate. *Materials Science and Engineering: A* 2021; 804: 140753.
57. Ramos AS, Simões S, Maj L, Morgiel J, Vieira MT. Effect of deposition parameters on the reactivity of Al/Ni multilayer thin films. *Coatings* 2020; 10: 721.
58. MatWeb. Nickel, Ni.  
<https://www.matweb.com/search/DataSheet.aspx?MatGUID=e6eb83327e534850a062dbca3bc758dc> (8 September 2023, date last accessed).
59. MatWeb. Titanium, Ti.  
<https://www.matweb.com/search/DataSheet.aspx?MatGUID=66a15d609a3f4c829cb6ad08f0dafc01> (8 September 2023, date last accessed).
60. MatWeb. Nitinol - NiTi Shape Memory Alloy; High-Temperature Phase.  
<https://www.matweb.com/search/DataSheet.aspx?MatGUID=de9dd08433714f698d513766dceca437> (8 September 2023, date last accessed).
61. Gall K, Juntunen K, Maier HJ, Sehitoglu H, Chumlyakov YI. Instrumented Micro-Indentation of NiTi Shape-Memory Alloys. *Acta Materialia* 2001; 49: 3205–3217.